

Special Section:

Investigations of Vera Rubin Ridge, Gale Crater

Key Points:

- High sanidine (full Al,Si structural disorder) and specular hematite hydrothermally precipitated on basaltic Maunakea volcano, Hawai'i
- Smectite and 10-Å phyllosilicate (both Mg-rich) also hydrothermally precipitated as diagenetic phases
- High sanidine and specular hematite at Gale crater can result from diagenetic alteration of basaltic compositions by hydrothermal fluids

Supporting Information:

- Supporting Information S1
- Data Set S1
- Data Set S2
- Data Set S3

Correspondence to:

R. V. Morris,
richard.v.morris@nasa.gov

Citation:

Morris, R. V., Rampe, E. B., Vaniman, D. T., Christoffersen, R., Yen, A. S., Morrison, S. M., et al. (2020). Hydrothermal precipitation of sanidine (adularia) having full Al,Si structural disorder and specular hematite at Maunakea volcano (Hawai'i) and at Gale Crater (Mars). *Journal of Geophysical Research: Planets*, 125, e2019JE006324. <https://doi.org/10.1029/2019JE006324>

Received 9 DEC 2019

Accepted 27 MAY 2020

Accepted article online 19 JUN 2020

©2020. The Authors.

This is an open access article under the terms of the Creative Commons Attribution-NonCommercial-NoDerivs License, which permits use and distribution in any medium, provided the original work is properly cited, the use is non-commercial and no modifications or adaptations are made.

Hydrothermal Precipitation of Sanidine (Adularia) Having Full Al,Si Structural Disorder and Specular Hematite at Maunakea Volcano (Hawai'i) and at Gale Crater (Mars)

R. V. Morris¹ , E. B. Rampe¹ , D. T. Vaniman² , R. Christoffersen³, A. S. Yen⁴ , S. M. Morrison⁵ , D. W. Ming¹ , C. N. Achilles⁶ , A. A. Fraeman⁴ , L. Le³, V. M. Tu³, J. P. Ott⁷, A. H. Treiman⁸ , J. V. Hogancamp³, T. G. Graff³, M. Adams⁹, J. C. Hamilton⁹, S. A. Mertzman¹⁰ , T. F. Bristow¹¹ , D. F. Blake¹¹, N. Castle¹¹ , S. J. Chipera¹², P. I. Craig² , D. J. Des Marais¹¹ , G. Downs¹³, R. T. Downs¹³, R. M. Hazen⁵, J.-M. Morookian⁴, and M. Thorpe¹ 

¹NASA Johnson Space Center, Houston, TX, USA, ²Planetary Science Institute, Tucson, AZ, USA, ³Jacobs, NASA Johnson Space Center, Houston, TX, USA, ⁴Jet Propulsion Laboratory, California Institute of Technology, Pasadena, CA, USA, ⁵Carnegie Institution for Science, Washington, DC, USA, ⁶NASA Goddard Spaceflight Center, Greenbelt, MD, USA, ⁷Harvard University, Cambridge, MA, USA, ⁸Lunar and Planetary Institute/USRA, Houston, TX, USA, ⁹Department of Physics and Astronomy, University of Hawai'i at Hilo, Hilo, HI, USA, ¹⁰Franklin and Marshall College, Lancaster, PA, USA, ¹¹NASA Ames Research Center, Moffett Field, CA, USA, ¹²CHK Energy, Oklahoma City, OK, USA, ¹³Department of Geosciences, University of Arizona, Tucson, AZ, USA

Abstract Hydrothermal high sanidine and specular hematite are found within ferric-rich and gray-colored cemented basaltic breccia occurring within horizontal, weathering-resistant strata exposed in an erosional gully of the Pu'u Poliahu cinder cone in the summit region of Maunakea volcano (Hawai'i). The cone was extensively altered by hydrothermal, acid-sulfate fluids at temperatures up to ~400 °C, and, within strata, plagioclase was removed by dissolution from progenitor Hawaiitic basalt, and sanidine and hematite were precipitated. Fe₂O₃T concentration and Fe³⁺/ΣFe redox state are ~12 wt.% and ~0.4 for progenitor basalt and 46–60 wt.% and ~1.0 for cemented breccias, respectively, implying open-system alteration and oxid precipitation. Hydrothermal high sanidine (adularia) is characterized by full Al,Si structural disorder and monoclinic unit-cell (Rietveld refinement): $a = 8.563(19) \text{ \AA}$, $b = 13.040(6) \text{ \AA}$, $c = 7.169(4) \text{ \AA}$, $\beta = 116.02(10)^\circ$, and $V = 719.4(19) \text{ \AA}^3$. Hematite (structure confirmed by Rietveld refinement) is the predominant Fe-bearing phase detected. Coarse size fractions of powdered hematite-rich breccia (500–1000 μm) are dark and spectrally neutral at visible wavelengths, confirming specular hematite, and SEM images show platy to polyhedral hematite morphologies with longest dimensions >10 μm. Smectite and 10-Å phyllosilicate, both chemically dominated by Mg as octahedral cation, are additional diagenetic hydrothermal alteration products. By analogy and as a working hypothesis, high sanidine (Kimberly formation) and specular hematite (Mt. Sharp group at Hartmann's Valley and Vera Rubin ridge) at Gale crater are interpreted as diagenetic alteration products of Martian basaltic material by hydrothermal processes.

Plain Language Summary A layer of weathering-resistant material is located within the walls of an erosional gully of the Pu'u Poliahu cinder cone in the summit region of Maunakea volcano (Hawai'i). The volcanic cone, initially composed of unaltered basaltic material (tephra), was extensively altered throughout by hot, sulfuric-acid solutions. The layer is a location where the alteration by hot water was particularly aggressive, cementing the volcanic sediment and causing extensive chemical and mineralogical changes. Instead of basaltic chemical and mineralogical compositions, altered tephra was enriched in iron from aqueous precipitation of the mineral hematite (Fe₂O₃) and was characterized by high sanidine with full structural disorder as the feldspar (instead of plagioclase, which was removed by dissolution) and by Mg-rich phyllosilicates as additional precipitation products. Hematite, often present as a red pigment in geologic materials, was precipitated from the hot water as specular (i.e., gray) hematite. By analogy, high sanidine and specular hematite at Gale crater

(Mars) can be interpreted as alteration products of preexisting Martian basaltic sediment by hot-water solutions.

1. Introduction

The Mars Science Laboratory (MSL) rover *Curiosity* continues to study ancient (~3.5 Ga) fluviolacustrine rocks since landing in Gale crater in August 2012, with identification of potentially habitable environments a primary mission goal (e.g., Grotzinger et al., 2012). The mineralogy, major, minor, and volatile element chemistry, and isotopic compositions and their variations across the Martian surface are critical for understanding its present state, the mineralogical and chemical characteristics of past aqueous environments, and the processes that modified the surface to its present state. To date, *Curiosity* has traversed more than ~350 m of vertical elevation.

The transmission X-ray diffraction (XRD) instrument CheMin onboard *Curiosity* (Blake et al., 2012) acquires patterns from powders of drilled rock samples whose quantitative analyses identified primary minerals (e.g., plagioclase, olivine, pyroxene, and tridymite), secondary materials (e.g., hematite, sulfates, opal-A, opal-CT, and phyllosilicates), crossover minerals (e.g., magnetite and K-feldspar; $KAlSi_3O_8$ for the stoichiometric composition), and XRD-amorphous phases. This paper focuses on CheMin detections of monoclinic high sanidine (K-feldspar) having full Al,Si structural disorder, specular (gray colored) hematite ($\alpha\text{-Fe}_2\text{O}_3$), and the working hypothesis that the two minerals are products of hydrothermal activity. The name “high sanidine” refers to structural state and implies no specific formation mode.

The drill sample “Windjana,” obtained at the Kimberly formation (Bradbury group) on the plains of Gale crater, has to date the highest concentration of feldspar as high sanidine (~26 wt.% compared to ~6 wt.% plagioclase) for the crystalline mineral fraction (Treiman et al., 2016; revised by Morrison et al., 2018). For all other drill samples on the plains of Gale crater through Vera Rubin ridge (VRR) on Mt. Sharp, plagioclase (~andesine) is the dominant feldspar: “John Klein,” “Cumberland,” “Confidence Hills,” “Telegraph Peak,” “Buckskin,” “Marimba,” “Quela,” “Sebina,” “Duluth,” “Stoer,” and “Highfield” have 3 to 9 wt.% sanidine and 38–56 wt.% plagioclase; and “Mojave2,” “Big Sky,” “Greenhorn,” “Lubango,” “Okoruso,” “Oudam,” and “Rock Hall” have no detectable sanidine and 38 to 55 wt.% plagioclase (Achilles et al., 2020; Bristow et al., 2018; Morrison et al., 2018; Rampe et al., 2017, 2020; Yen et al., 2017).

Treiman et al. (2016) developed hypotheses for both igneous and nonigneous origins for Windjana high sanidine. The authors favored igneous origins largely on the basis of chemical arguments, considering Windjana sandstone to be a cemented mixture of volcanic components from different sources with trachyte being the sanidine-bearing component. The authors also considered potassic metasomatic and diagenetic alteration as Windjana sanidine formation pathways but considered them less likely on the basis of differences in mineral assemblages between the Windjana sample and those resulting from terrestrial potassic metasomatic and diagenetic alteration.

Crystalline hematite was detected by CheMin in all drill samples listed above except Cumberland, John Klein, and Buckskin and is the dominant ferric oxide/oxyhydroxide detected by CheMin to date (above references). Of the hematite-bearing drill samples, Oudam and Highfield (Murray formation, Hartmann's Valley, and Jura member, respectively) from the base of Mt. Sharp and Vera Rubin ridge, respectively, have evidence from color images and spectroscopy (Achilles et al., 2020; Fraeman et al., 2020; Horgan et al., 2019) for specular (gray) hematite; for other drill samples, the corresponding evidence is for pigmentary (red) hematite.

To examine and test the working hypothesis that high sanidine (specifically, the Windjana drill sample; Treiman et al., 2016) and specular hematite (specifically, Oudam and Highfield drill samples; Achilles et al., 2020; Fraeman et al., 2020; Horgan et al., 2019; Rampe et al., 2020) are products of local hydrothermal activity at Gale crater, we analyzed, as an analog, samples from gray regions of cemented breccia that occur as horizontal strata exposed in an erosional gully of a cinder cone (Pu'u Poliahu) located in the summit region of Maunakea volcano (Hawai'i) (Figure 1). The cone's basaltic tephra has been extensively altered by hydrothermal, acid-sulfate fluids (e.g., Morris et al., 2000; Wolfe et al., 1997), and the strata are more resistant to weathering, giving them the appearance of a ridge. Samples of relatively unaltered tephra, collected upslope from the strata, and a gray float rock from the gully floor were also analyzed. Attribution of the gray

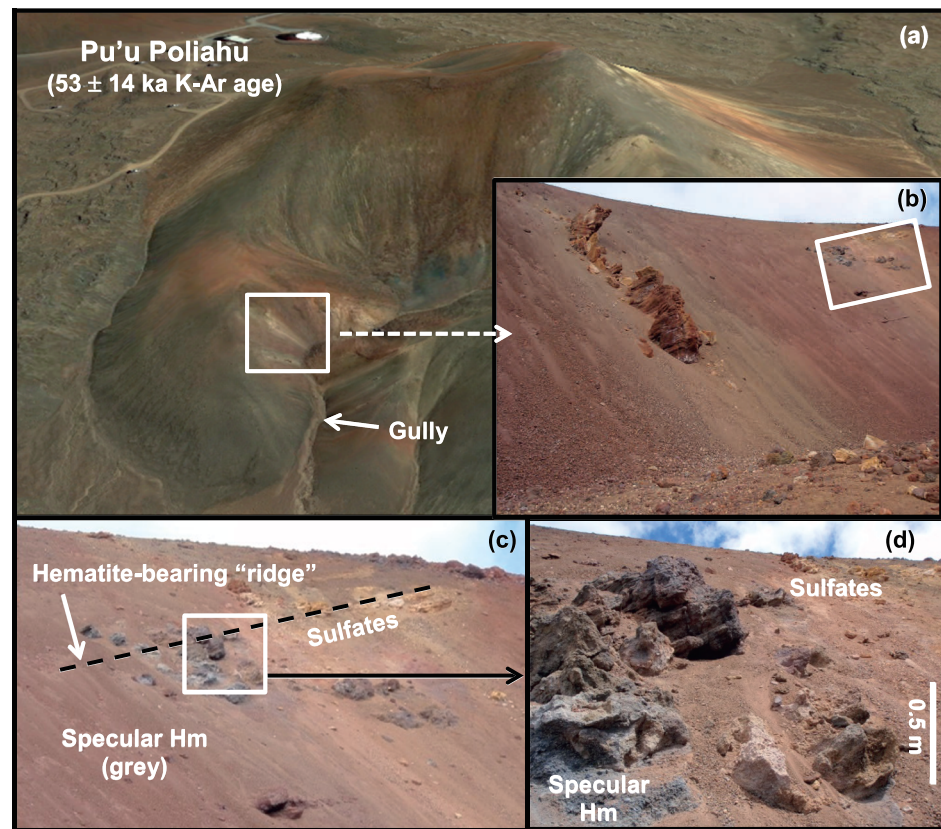


Figure 1. (a) Pu'u Poliahu cinder cone in the summit region of Maunakea volcano that has undergone extensive alteration by acid-sulfate fluids and vapors (Wolfe et al., 1997). (b) View of weathering-resistant “ridge” exposed in wall of erosional gully. (c) Color of exposed ridge is dominated by specular hematite (gray, left) and by sulfate phases and kaolinite (white to yellow, right). (d) Expanded view of (c) showing a sampling location for specular hematite. Scale bar in (d) pertains to foreground rocks.

color to specular hematite was obvious in the field, and preliminary analyses confirmed the mineralogy and revealed Fe_2O_3 -rich chemical compositions and high sanidine interpreted as a hydrothermal alteration product. Sulfate minerals (e.g., alunite and jarosite), phyllosilicates (e.g., smectite and kaolinite), red hematite, and poorly crystalline phases have been previously reported as alteration products in samples collected across the Maunakea summit region (e.g., Berger et al., 2020; Golden et al., 1993; Guinness et al., 2007; Hamilton et al., 2008; Morris et al., 1996, 2000, 2005). Specular hematite as spherules was reported within a breccia (float rock) from the floor of the Pu'u Poliahu gully (Morris et al., 2005).

In keeping with frequent literature usage (e.g., Smith & Brown, 1988), we will refer to hydrothermal K-feldspar as “adularia” with no implications as to its structural state. Similarly, “specular hematite” includes “black or gray hematite” (to make a color distinction with pigmentary red hematite) and “micaceous hematite” which is specular hematite having a platy morphology. We report Rietveld analysis of XRD powder diffraction patterns, bulk chemistry by X-ray fluorescence (XRF), mineral chemistry by electron microprobe analysis (EMPA), and morphology, chemical maps, qualitative chemical analyses from Scanning Electron Microscopy (SEM) images and selective-area energy-dispersive X-ray (EDX) analysis, and visible, near-IR spectra (~400–1000 nm).

2. Samples and Methods

2.1. Maunakea Samples

Gray-colored hand samples from Pu'u Poliahu were obtained as a float rock (HWMK125) from the gully floor in 2001 and from the horizontal strata of coherent (cemented) breccia exposed in the erosional gully in 2013 (HW13MK001, HW13MK011A, HW13MK030, HW13MK030B, HW13MK030C, and HW13MK030D)

(Figure 1). A float rock of progenitor basalt (HW13MK021) was collected upslope near the gully ridge. Representative whole-rock samples were used for major element analyses, dry ground and sieved into <150, 150–500, 500–1000, and <1000 μm size fractions using Ni metal sieves with square holes for XRD, and visible, near-IR analyses, and prepared as polished mounts for microanalysis (EMPA and SEM). Drill samples were obtained for two Maunakea rocks (HW13MK001 and HM13MK030) by dry drilling under ambient laboratory conditions with an MSL analogue drill and bit (rotary percussion drill and 0.5-in tungsten-carbide bit with a flat end). Hematite powders previously analyzed by Morris et al. (1985) and Lane et al. (2002) for spectral properties were reanalyzed here for consistency in instrument and measurement geometry.

2.2. Analyses at Johnson Space Center

Powder XRD patterns were obtained under ambient laboratory conditions with a PANalytical X'Pert Pro instrument configured with $\text{CoK}\alpha$ radiation and spinner stage. Whole-rock powders, pulverized with mortar and pestle to pass a <150 μm sieve), were spiked with positional standards (~15 wt.% each of NIST Si metal and Cr_2O_3 with respect to bulk mixture), and unit-cell parameters and phase abundances were calculated from Rietveld refinements between $5^\circ 2\theta$ and $80^\circ 2\theta$ using JADE© software (Materials Data Inc.). For samples containing smectite, the (001) and (02 ℓ) smectite peaks were excluded from the fits. A linear background was included, and a Pearson-VII profile shape function was used for all phases. The unit-cell parameters, full-width at half maximum, skewness/asymmetry term s_0 , and exponent/Lorentzian term p_0 were allowed to refine for all phases. Specimen displacement was adjusted until the unit-cell parameters of the Si and Cr_2O_3 standards were closest to the reported NIST values (reference 640e for Si and reference 674b for Cr_2O_3 ; <https://www.nist.gov/programs-projects/powder-diffraction-srms>).

Reflectance spectra (350–2500 nm) were obtained on sample powders (<150 and 500–1000 μm size fractions) under ambient conditions with a fiber-optic ASD FieldSpec 3 spectrometer configured with a MUGLite attachment (Malvern-PANalytical). According to the manufacturer, spectral resolutions are 3 nm at 700 nm, 8.5 nm at 1400 nm, and 6.5 nm at 2100 nm. Samples were irradiated with a polychromatic (incandescent) light source located in a parabolic reflector, for which the axes of the reflector and fiber-optic pickup make 55° and 78° angles, respectively, from the viewing plane in a plane normal to it. Reflectance was calibrated against a Spectralon white standard (Labsphere SRS-99-010). Only the spectral region between 400 and 1000 nm, which spans the spectral range of MSL Mastcam multispectral and ChemCam passive instruments, is discussed in this paper.

Point and scan analyses for major elements were acquired on a CAMECA SX-100 electron microprobe operating at 15 kV, 20 nA, 5 μm beam size, and 30 s integration time per element. SEM images and EDX analyses were acquired with a JEOL JSM-7600F field emission SEM operating at 15 kV and 30 nA and configured with a Thermo NSS SSD detector. Using Environment for Visualizing Images software (L3Harris Geospatial), individual SEM backscattered electron (BSE) and element maps were put into an “element cube” so that a “z axis” profile gave a histogram of relative element concentrations for any selection of map pixels.

2.3. Elemental and Redox Analyses at Franklin and Marshall College

Sample weight loss on ignition (LOI) was measured by heating an aliquot of sample powder in air at 950°C in air for at least 1 hr. Major element chemistry was determined for LOI residues by XRF using a 9:1 $\text{Li}_2\text{B}_4\text{O}_7$: sample flux-fusion procedure to prepare glass disks and a Philips 2404 XRF spectrometer configured with a 4 kW Rh X-ray tube (cf. Boyd & Mertzman, 1987). Because analyses were done on LOI residues fired in air, total Fe is reported as $\text{Fe}_2\text{O}_3\text{T}$ and total S as SO_3R , recognizing that most common sulfates (except CaSO_4) undergo SO_3 loss during LOI heating. The SO_3 concentration of bulk samples (SO_3T) was measured by XRF using a pressed pellet of unheated powder. The amount of Fe^{2+} was measured on unheated samples using the Reichen and Fahey (1962) procedure modified by including a titration of NBS geochemical standard rock NBS-688 and multiplying titrated sample FeO concentrations by the ratio of the titrated NBS-688 value to its standard value (7.64 wt.% FeO; Gladney et al., 1987). The measurements and calculation account for slight differences in acid concentrations and other vagaries in the technique. Concentrations of Fe^{3+} were calculated by differences with total Fe concentrations.

Table 1
Bulk Chemical Compositions

Sample (wt.%)	Average Basalt ^a	HW13MK021 ^b	HW13MK001 ^c	HW13MK030 ^c	HW13MK030B ^c	HW13MK030C ^c	HW13MK125 ^d
<i>Measurements on Loss-on-Ignition (LOI) Residue (950 °C in air)</i>							
SiO ₂	49.74	50.88	25.94	30.73	21.41	25.40	24.97
TiO ₂	2.77	2.41	1.29	1.48	1.04	1.33	1.25
Al ₂ O ₃	17.35	17.69	8.37	10.29	6.84	7.98	8.05
Cr ₂ O ₃	0.00	0.01	0.01	0.00	0.01	0.00	0.01
Fe ₂ O ₃ T	12.03	11.30	50.70	45.64	59.85	51.42	50.97
MnO	0.21	0.22	0.39	0.66	0.37	0.49	1.19
MgO	3.93	3.36	7.13	2.46	4.92	7.85	7.38
CaO	6.60	6.43	1.59	1.46	1.37	2.26	1.98
Na ₂ O	4.33	4.64	0.94	1.36	0.80	0.89	0.89
K ₂ O	1.90	2.04	2.85	4.82	2.31	1.43	1.93
P ₂ O ₅	0.85	1.08	0.55	0.58	0.41	0.55	0.56
SO ₃ R	n.d.	0.19	0.15	0.20	0.31	0.20	0.06
Total	99.71	100.24	99.90	99.68	99.64	99.80	99.24
<i>Measurements on Bulk Sample</i>							
%LOI	1.60	0.53	4.68	1.29	2.21	3.90	2.36
FeO	6.02	6.13	0.17	0.54	1.17	0.49	0.00
Fe ₂ O ₃ ^e	5.34	4.49	50.51	45.04	58.55	50.88	50.97
SO ₃	0.094	0.35	0.29	0.25	0.38	0.20	0.26
Fe ³⁺ /∑Fe ^f	0.44	0.40	1.00	0.99	0.98	0.99	1.00

^aAverage Hawaiitic basalt composition from Morris et al. (2000). ^bFloat rock upslope from cemented breccias on Pu'u Poliahu gully crest. ^cGray cemented breccia from Pu'u Poliahu "ridge" (see Figure 1). ^dGray cemented float rock from Pu'u Poliahu gully floor. ^eCalculated by difference from FeO and Fe₂O₃T. ^fCalculated from total Fe concentration and Fe³⁺ concentration from difference of total and Fe²⁺ concentrations.

3. Chemistry and Mineralogy

3.1. Bulk Chemical Composition

The bulk chemical compositions of average Hawaiitic basalt (Morris et al., 2000) and Pu'u Poliahu samples are given in Table 1. Progenitor basalt HW13MK021 is essentially isochemical with that for average Hawaiitic basalt, and its redox state (Fe³⁺/∑Fe = 0.40) is consistent with minimal chemical and mineralogical alteration. The remaining HW13MK samples are strongly chemically and mineralogically altered (oxidized) relative to average Hawaiitic basalt (e.g., Fe₂O₃T = 46–60 wt.% compared to 12 wt.% for the unaltered sample and Fe³⁺/∑Fe = 0.98–1.00 compared to 0.40). Variations in Tau values across the major elements relative to HW13MK021 as progenitor are shown in Figure 2 as a Tau histogram, where (Tau)_a = [(S_a/S_Z) × (P_Z/P_a) – 1.0], S_Z and P_Z are TiO₂ concentrations for sample and progenitor, respectively, and S_a and P_a

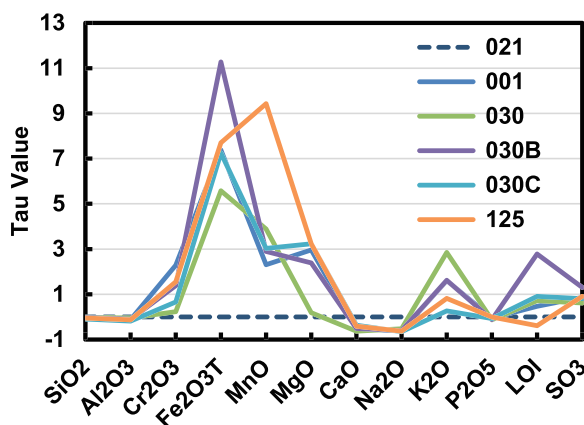


Figure 2. Tau histograms for HW13MK Maunakea rocks calculated with respect to a HW13MK021 progenitor.

are the concentrations of major oxides/elements (i.e., a = SiO₂, Al₂O₃, Cr₂O₃, and Fe₂O₃T) for sample and progenitor, respectively (all concentrations in wt.%). Tau values represent mass gains or losses of elements in a sample relative to known (or presumed) progenitor values using a mass balance relative to an immobile element (TiO₂) (Anderson et al., 2002; Brimhall & Dietrich, 1987). Note that (Tau)_a = 0.0 for a = TiO₂ and that (Tau)_a = –1.0 when S_a = 0.0 wt.% (e.g., S_{CaO} = 0.0 wt.%). For isochemical alteration, (Tau)_a = 0.0 for all oxides/elements. A characteristic of Tau values is that normalization of bulk concentrations to exclude any chemical component (e.g., SO₃ + Cl or CaSO₄) or to include any chemical component (e.g., SiO₂) does not change Tau values for the remaining components as long as the excluded/included component has TiO₂ = 0.0 wt.%.

Although evident by inspection of chemical data in Table 1 and ignoring elements with relatively small concentrations (Cr₂O₃, MnO, and P₂O₅), the Tau histogram (Figure 2) shows significant element gains for MgO, K₂O, and especially Fe₂O₃T, significant element losses for CaO and

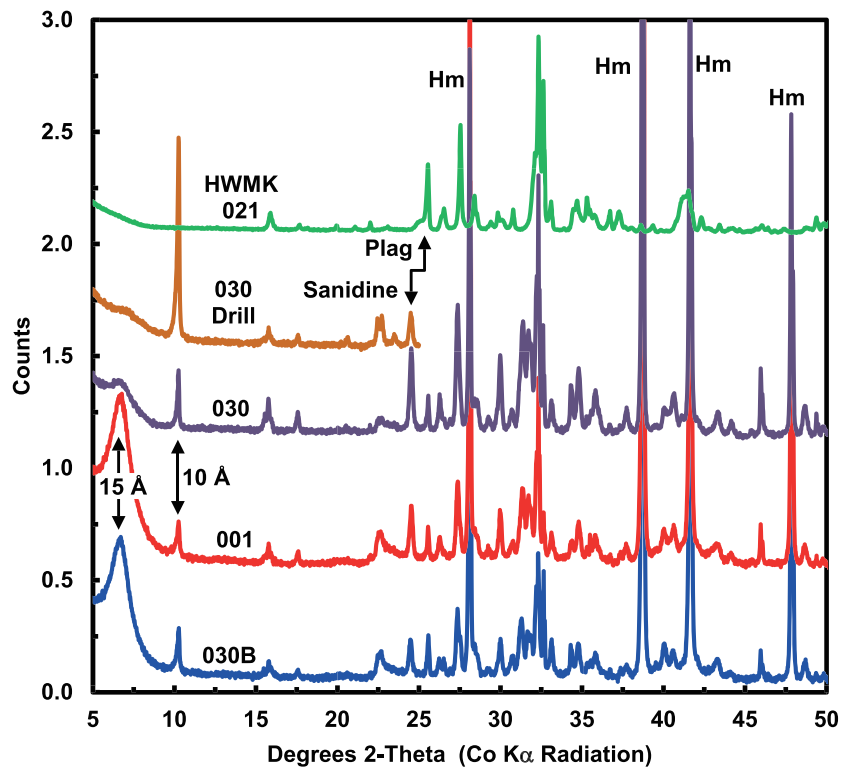


Figure 3. XRD patterns for weakly altered basalt (HW13MK021) and hydrothermally altered basalts HW13MK001, 030Drill, 030, and 030B. The HW13MK030Drill pattern is truncated at 25° 2θ to prevent pattern overlap at $2\theta > 25^\circ$. Hm = hematite; Plag = plagioclase.

Na_2O , and some element loss for SiO_2 and Al_2O_3 . Considering that $\text{Fe}^{3+}/\sum\text{Fe} \sim 1.0$ for the altered samples (Table 1) and, anticipating results discussed later, the Tau histogram points to K-feldspar (KAlSi_3O_8) rather than plagioclase (e.g., andesine $\sim\text{Na}_{0.6}\text{Ca}_{0.4}\text{Al}_{1.4}\text{Si}_{2.6}\text{O}_8$) as the dominant feldspar and to hematite for $\text{Fe}_2\text{O}_3\text{T}$. Significant mass gains for MgO are present in three of four altered samples, but the MgO speciation associated with the mass gain is not apparent from Figure 2.

3.2. X-Ray Diffraction: Overview

Representative Maunakea powder X-ray diffraction patterns are shown in Figure 3, and crystalline phase assignments, relative abundances, and unit-cell parameters from Rietveld refinements are given in Tables 2 and 3. Unit-cell parameters are the average values of separate co-author refinements, and parameter uncertainties are standard deviations of average values.

The XRD pattern for and Rietveld refinement of HW13MK021 are characteristic of an igneous assemblage that underwent minimal mineralogical alteration in addition to being chemically unaltered as discussed above. Its XRD pattern is dominated by plagioclase (~ 77 wt.%). Phyllosilicate basal reflection peaks near 15, 10, and 7 Å are not detected, consistent with the absence of phyllosilicates. The remaining Pu'u Poliahu samples (HW13MK-001, -011A, -030, -030B, -030D, and -030Drill and HWMK125), as expected from their bulk chemistry and redox state (Table 1), are products of extensive oxidative mineralogical alteration. With respect to crystalline minerals, hematite ($\alpha\text{-Fe}_2\text{O}_3$) is the most abundant (43–61 wt.%) and feldspar is present as K-feldspar (0–29 wt.% as monoclinic high sanidine) and plagioclase (10–50 wt.%). A phyllosilicate with a sharp, 10-Å basal reflection is present (2–25 wt.%) in four of five hematite-rich samples (Table 2 and Figure 4), and an ~ 15 -Å basal reflection most evident in HW13MK-001 and -030B (Figure 4a) shows one or more fully expanded smectites are also present. Phase chemistry inferred from XRD unit-cell parameters was confirmed by microanalysis for feldspars and hematite, but specific chemical compositions were not rigorously coupled with smectite and 10-Å phyllosilicates.

Table 2
Rietveld Crystalline Phase Abundances

Sample	HW13MK021	HW13MK001	HW13MK011A	HW13MK030	HW13MK030B	HWMK030D	HW13MK030Drill	HWMK125
Plagioclase	77(1)	18(1)	50(1)	14(1)	14(1)	10(1)	10(1)	26(1)
Sanidine	2(1)	19(1)	0	29(1)	11(1)	20(1)	14(1)	10(1)
Forsterite	9(1)	0	0	0	0	0	0	0
Pyroxene	6(1)	0	0	0	0	0	0	0
(Ti)Magnetite	6(1)	0	0	0	0	0	0	0
10 Å-Phase	0	2(1)	0	8(1)	7(1)	15(1)	25(1)	7(1)
Hematite	0	56(1)	48(1)	43(1)	61(5)	49(1)	51(3)	57(1)
Other	0	5	4	6	7	6	0	0
Total	100	100	100	100	100	100	100	100

Note. Numbers in parenthesis are uncertainties of final digit(s) as average standard deviations.

3.3. XRD: K-Feldspar

The alkali feldspar quadrilateral diagram (**b** versus **c** unit-cell lengths) shows data for Maunakea plagioclase and K-feldspar (Figure 5a; data from supporting information). Ideal end-member coordinates for low and high albite and low microcline are from Kroll and Ribbe (1987), and those for ideal high sanidine are from Ferguson et al. (1991) who represent their cell parameters (**b** = 13.046 Å, **c** = 7.175 Å) to correspond to the maximum Al,Si structural disorder possible for $KAlSi_3O_8$. Other (**b**, **c**) coordinates used for ideal high sanidine in the literature include (in Å) (13.040, 7.173) (Grove & Hazen, 1974); (13.041, 7.171), (13.044, 7.165), and (13.047, 7.161) (Černý & Chapman, 1986); (13.031, 7.177) (Kroll & Ribbe, 1987); (13.028, 7.17) (Scambos et al., 1987); and (13.032, 7.180) (Angel et al. (1988). Ideal high sanidine, that is sanidine with full Al,Si structural disorder, is characterized by random distribution of Al and Si atoms at the four equivalent tetrahedral sites in a three-to-one ratio and is stable at temperatures >900 °C (e.g., Parsons et al., 2015). Maunakea **b-c** data for sanidine (average: **b** = 13.040(6) Å, **c** = 7.169(4) Å) cluster near ideal high sanidine. The **b-c** data for Maunakea plagioclase cluster near the literature value for andesine (andesine coordinates from Fitz Gerald et al. (1986; **b** = 12.880 Å, **c** = 7.112 Å).

Although only sanidine data for Windjana are plotted, Gale crater drill samples show a similar plagioclase-sanidine relationship (Figure 5a) (Achilles et al., 2020; Morrison et al., 2018; Rampe et al., 2020). We reexamined CheMin XRD patterns for all other sanidine-bearing samples, and they contained only minor amounts of sanidine which prevented calculation of reliable Rietveld unit-cell parameters. Only Windjana has sanidine peaks with well-defined positions (maxima) because nearby plagioclase peaks have lower intensities. Similarly, unit-cell lengths for plagioclase are not plotted for Windjana because its XRD peaks have low intensity compared to nearby sanidine peaks.

Černý and Chapman (1986) note that “High nucleation and crystallization rates at low temperatures favor the metastable precipitation of totally disordered adularia, which must be subsequently shielded against order-promoting agents to preserve the original structural state.” Maximum Al,Si disorder tends to be present for fine-grained adularia, which is a manifestation of the fast nucleation and rapid precipitation that

Table 3
Average Unit-Cell Parameters for Crystalline Phases From Rietveld Analysis for Maunakea Samples

Phase	Crystal system	a (Å)	b (Å)	c (Å)	α (°)	β (°)	γ (°)	V (Å ³)
Sanidine	MC (C2/m)	8.563(19)	13.040(6)	7.169(4)	90	116.02(10)	90	719.4(19)
Plagioclase	TC (C-1)	8.180(9)	12.877(8)	7.120(5)	93.47(29)	116.30(5)	90.11(20)	670.8(11)
Hematite	HEX (R-3c)	5.035(1)	5.035(1)	13.746(2)	90	120	90	301.8(2)
10 Å-Phase	MC (C2/m)	5.313(12)	9.188(21)	10.150(6)	90	99.63(28)	90	488.5(10)
Pyroxene	MC (C2/c)	9.670(1)	8.820(1)	5.324(1)	90	107.90(07)	90	443.7(7)
Olivine	ORTH (Pbnm)	4.790(1)	10.335(1)	6.029(6)	90	90	90	298.4(3)
(Ti)Magnetite	CUB (Fd-3 m)	8.450(6)	8.450(6)	8.450(6)	90	90	90	603.4(13)

Note. Pyroxene and olivine unit-cell parameter from HW13MK021. Numbers in parenthesis are uncertainties of final digit(s) as average standard deviations. MC = monoclinic; TC = triclinic; HEX = hexagonal; ORTH = orthorhombic; CUB = cubic.

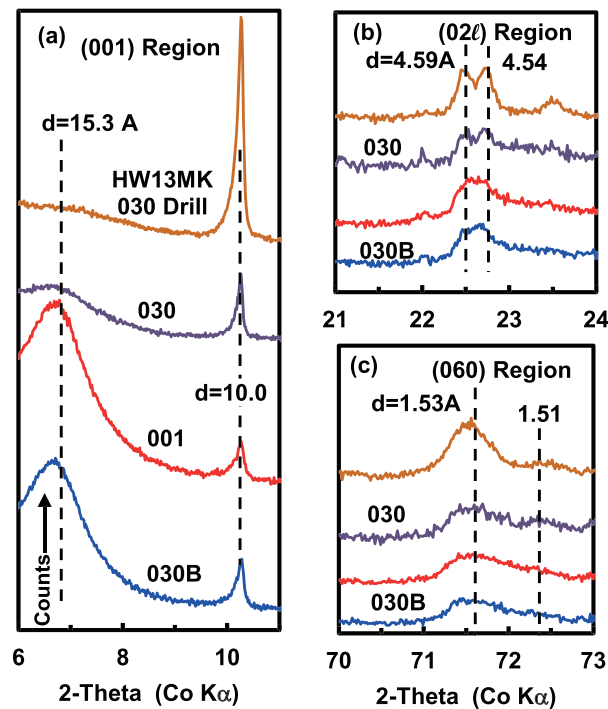


Figure 4. XRD patterns at room temperature and ambient laboratory air. (a) Basal reflection peaks (001) at 15.3 Å (expanded smectite) and 10.0 Å (possible tri-octahedral mica). (b) The (02ℓ) reflection peaks at 4.59 and 4.54 Å from trioctahedral and dioctahedral phyllosilicates. (c) The (060) reflection peaks at 1.53 and 1.51 Å from trioctahedral and dioctahedral phyllosilicates.

favors the metastable structural state with full Al,Si disorder (e.g., Černý & Chapman, 1984, 1986). As shown later, SEM images show Maunakea adularia is fine grained, consistent with XRD observation of full Al,Si structural disorder.

Pyrogenetic sanidine (i.e., magmatic sanidine or preexisting sanidine heated to high temperatures regardless of thermal source) characterized by high degrees of Al,Si structural disorder occur naturally but result from atypical circumstances. Scambos et al. (1987) infer that the cooling rate during ascent for a coesite-sanidine kimberlite nodule was sufficiently rapid to retain coesite and high sanidine with extreme Al,Si structural disorder. Alkali feldspars within granite xenoliths from lavas of the Nyiragongo volcano have extreme Al,Si structural disorder along the *b-c* join between high sanidine and high albite through heating to high temperatures (above ~1000 °C) in magma of the volcano (Lehtinen & Sahama, 1981). Similarly, a xenolith from Kilbourne Hole (New Mexico) has high sanidine with extreme structural disorder attributed to xenolith heating when incorporated into the basaltic magma (Grew, 1979). High sanidine with extreme structural disorder is reported in shock metamorphosed pegmatite from the Lake Lappajarvi impact structure (Finland) (Lehtinen, 1974).

In Figure 5b, we plot the high-sanidine corner of the alkali feldspar quadrilateral and include literature data for natural adularia formed in a range of hydrothermal settings, including alpine veins, nonalpine veins, and granitic pegmatites (Abad-Ortega et al., 1993; Černý et al., 2003; Černý & Chapman, 1984, 1986; Colville & Ribbe, 1968; Collerson, 1976; Deubener et al., 1991; Dong & Morrison, 1995; Emerson & Guidotti, 1974; Ferguson et al., 1991; Glazner, 1988; Guidotti et al., 1973; Harris et al., 1989; Lehtinen, 1974; Neusser et al., 2012; Norberg et al., 2014; Phillips & Ribbe, 1973; Scotford, 1969; Stewart & Wright, 1974; Zhou et al., 2001).

The figure demonstrates that sanidine with extreme-to-full structural Al,Si disorder occurs and is preserved in a variety of natural hydrothermal environments, including Maunakea volcano. The preservation time scale for adularia from certain Canadian granitic pegmatites is ~2.6 By (Černý & Chapman, 1984). For Maunakea adularia, the time-scale is the age of the volcano (~53 ka; Wolfe et al., 1997).

The *a* unit-cell length and unit-cell volume of alkali feldspars are more strongly dependent on chemical composition (i.e., K/Na ratio) than they are on Al,Si structural state and can be used to estimate molar Or concentrations (e.g., Orville, 1967; Stewart & Ribbe, 1969; Stewart & Wright, 1974), as shown in Figure 5c for naturally occurring samples from Maunakea, Windjana at Gale crater, and terrestrial samples representing diverse Al,Si structural states and geologic environments, including alpine and nonalpine veins, granitic pegmatites, volcanism (phenocrysts and xenocrysts), anatexites, plutons, and impact structures (citations in addition to those in the preceding paragraph: Angel et al., 1988; Blasi et al., 1982; Cherry & Trembath, 1978; Fox & Moore, 1969; Grew, 1979; Grove & Hazen, 1974; Hewlett, 1959; Kallaste, 2014; Kimata et al., 1996; Kroll & Ribbe, 1987; Lehtinen & Sahama, 1981; Menna et al., 2008; Orville, 1967; Scott et al., 1971; Scambos et al., 1987; Walter et al., 2013). Molar Or content was calculated from the unit-cell volume after Stewart and Wright (1974). For Maunakea high sanidine, the calculated molar Or ranges between ~80 and ~93 mole %.

The *b-c* plot in Figure 6 focuses on the geologic setting for K-feldspar for all samples included in Figure 5c. The Maunakea samples are characterized by high sanidine having Al,Si structural disorder that is comparable to the most extreme (i.e., highest values of *b*) previously reported in the literature, which are represented primarily by high sanidine precipitated from solutions associated with granitic pegmatites and epithermal deposits. Černý and Chapman (1984) cite precipitation temperatures near 250 °C for granitic pegmatites, and precipitation temperatures in the range ~150 to ~400 °C are inferred for epithermal vein deposits (e.g., Bethke et al., 2005; Castor et al., 2003; Dreher et al., 1998; Echavarría et al., 2006; Heald et al., 1987). Two

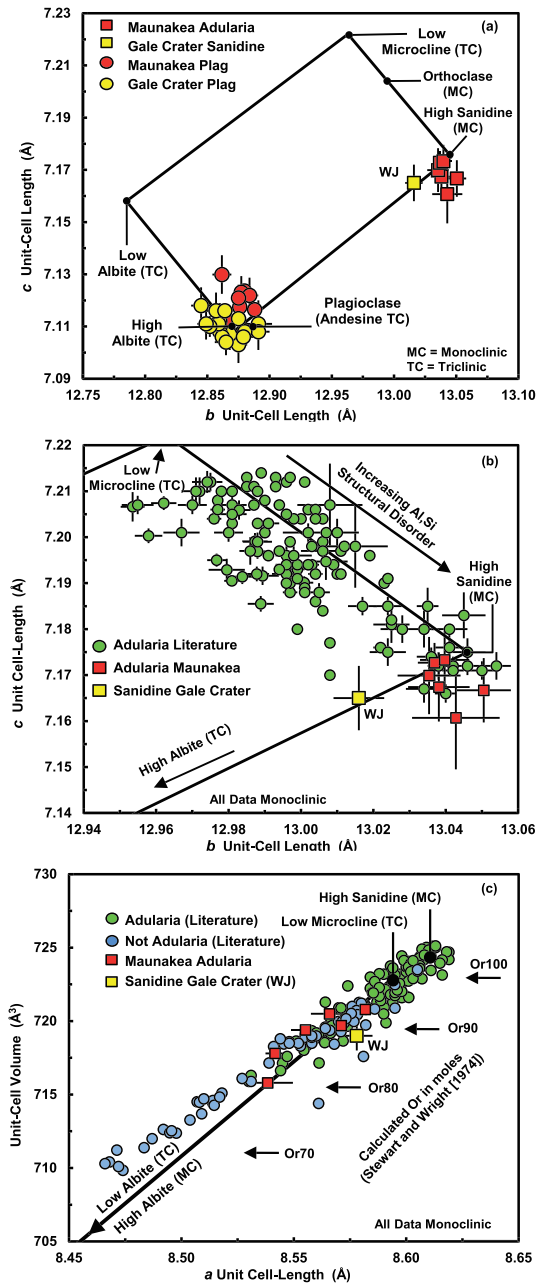


Figure 5. (a) Alkali-feldspar quadrilateral diagram (*b* versus *c* unit-cell lengths) for plagioclase and adularia from hydrothermally altered Maunakea tephra and for plagioclase and sanidine from drill samples at Gale Crater. (b) High-sanidine corner of the *b-c* quadrilateral comparing unit-cell parameters for Windjana (WJ) high-sanidine, adularia from Maunakea, and other monoclinic adularia the literature. (c) Monoclinic unit-cell length *a* versus unit-cell volume. The two parameters are more sensitive to alkali feldspar K/Na ratio than to Al,Si structural order; the solid line is defined by the alkali feldspar end-members. Mole percentage orthoclase calculated after Stewart and Wright (1974; their Equation 2).

the weighted molar fraction of the lattice parameters of the end-member phases (e.g., Denton & Ashcroft, 1991). Therefore, the calculation presumes that the two hematite samples actually have $\text{Al}_2\text{O}_3 = 0.0$ mole %.

other high sanidine occurrences have comparable extreme Al,Si structural states (Figure 6): (a) high sanidine from the Lake Lappajarvi impact structure (Finland) originating from shock-metamorphosed pegmatite and impact lava (Lehtinen, 1974) and (b) xenoliths that were exposed to magmatic temperatures and rapidly cooled (Grew, 1979; Lehtinen & Sahama, 1981; Scambos et al., 1987). Sanidine is also reported without unit-cell parameters at the Ries impact structure (e.g., Osinski, 2004) (refer to supporting information for numerical data, literature references, and other sample information).

3.4. XRD: Hematite, 10-Å Phyllosilicate, and Smectite

Rietveld refinements yielded unit-cell parameters for hematite and a 10-Å phyllosilicate identified as a mica group mineral (Table 3). The average unit-cell parameters for Maunakea hematite (Table 2) correspond within error to PDF #98-000-0240 ($a = 5.0355(5)$ Å, $c = 13.7471(7)$ Å, and $V = 301.88(7)$ Å³; Maslen et al., 1994) for hexagonal hematite. The unit-cell parameters for the 10-Å phyllosilicate (Table 3) are consistent with those for a ferrian tri-octahedral mica (Hazen et al., 1981; $a = 5.3290(9)$ Å, $b = 9.2300(15)$ Å, $c = 10.2191(11)$ Å, $\alpha = 90.00(1)$, $\beta = 99.98(1)$, $\gamma = 90.01(1)$, and $V = 495.0(1)$ Å³), but this specific mica identification is tentative without chemical confirmation (see below). The smectite is characterized by (001), (02ℓ), and (060) reflections at 15.3, ~4.59 to ~4.54, and 1.53 Å, respectively (Figure 4), and is dominantly trioctahedral on the basis of greater (060) intensity at 1.53 Å rather than at 1.51 Å.

Unit-cell lengths for Maunakea hematite are compared with corresponding literature and Gale crater data in a *c-a* plot (Figure 7). Literature data for natural and synthetic samples include crystallographic measurements of single crystals (Blake et al., 1966; PDF# 98-000-1032) and Rietveld refinements of patterns derived from hematite and hematite-bearing powders (Maslen et al., 1994; PDF# 98-000-0240; Gilbert et al., 2009; Lemine et al., 2010; Stękiel et al., 2015); red ochres (Jercher et al., 1998); coal bottom ash (Kniess et al., 2012); hematite from thermal decomposition of goethite ($\alpha\text{-FeOOH}$) and ferrihydrite (Alvarez et al., 2006; da Cunha & da Costa, 2016; Goss, 1987; Gilbert et al., 2009); Al-substituted (Das & Hendry, 2014; Li et al., 2016; Majzlan et al., 2002; Ruan & Gilkes, 1995), Mn-substituted (Alvarez et al., 2006; Wells et al., 2001), and Ti-substituted (Sorescu et al., 2010) hematite; and synthetic hematite from procedures designed to control hematite particle size (often nanoscale), morphology, and/or growth direction (Das & Hendry, 2014; Gilbert et al., 2009; Malik et al., 2014; Reufer et al., 2011). The black and red dashed lines were calculated from Vegard's Law between two hematite samples (Blake et al. [1966]: $a = 5.038(2)$ Å and $c = 13.772(12)$ Å) and Rampe et al. [2020]: $a = 5.042(3)$ Å and $c = 13.753(3)$ Å) and corundum (Thompson et al. [1987]: $a = 4.7586$ Å and $c = 12.9897$ Å). Unit-cell data for the former were derived from measurements on a hematite crystal, and corresponding data for the latter were derived from measurements on the drill sample Highfield (HF) at Gale crater. Vegard's law states that the lattice parameters of a solid solution between two phases having the same crystal structures and at the same temperatures are approximately

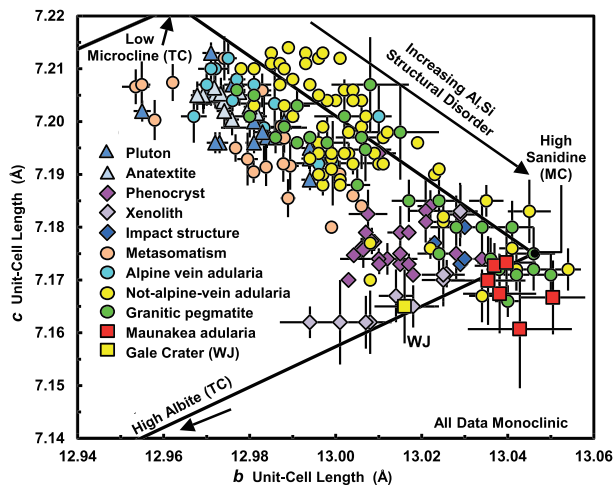


Figure 6. Alkali feldspar *b-c* unit-cell plot centered on the high-sanidine end-member comparing K-feldspar unit-cell lengths for Maunakea and Gale crater data with corresponding literature data for K-feldspar precipitated or crystallized in a variety of terrestrial environments. The plot includes only monoclinic K-feldspar. WJ = Windjana; TC = triclinic; MC = monoclinic.

As shown in Figure 7, unit-cell lengths for Maunakea hematite (red squares) are within the range of values for hematite without Al, Mn, and Ti as substitutional impurities (light-green and blue diamond symbols), consistent with their chemical compositions (Table 5). The Maunakea data cluster near the PDF0240 datum, which was derived from a synthetic hematite sample. The two Vegard lines show that Al-substituted hematite can follow the same trend as unsubstituted hematite. However, not all unit-cell data for Al-substituted hematite (cyan circles) follow Vegard's Law, although the general trend to shorter unit-cell length is present. Non-Vegard behavior for the hematite-corundum system is commonly observed even in controlled laboratory experiments because of the multiplicity of factors that influence unit-cell parameters (e.g., Stanjek & Schwertmann, 1992). Unit-cell data for Ti-hematite (gray circles) are present as a diffuse cluster that intermingles with other unit-cell data. The Gale crater drill samples will be discussed later. It is apparent from Figure 7 the range of unit-cell lengths for natural and synthetic hematite and hematite-bearing samples results from a multiplicity of factors, including the speciation and concentration of cationic and anionic substitutional impurities; discrete particle size, shape, strain, density, and porosity; and environmental conditions during and post

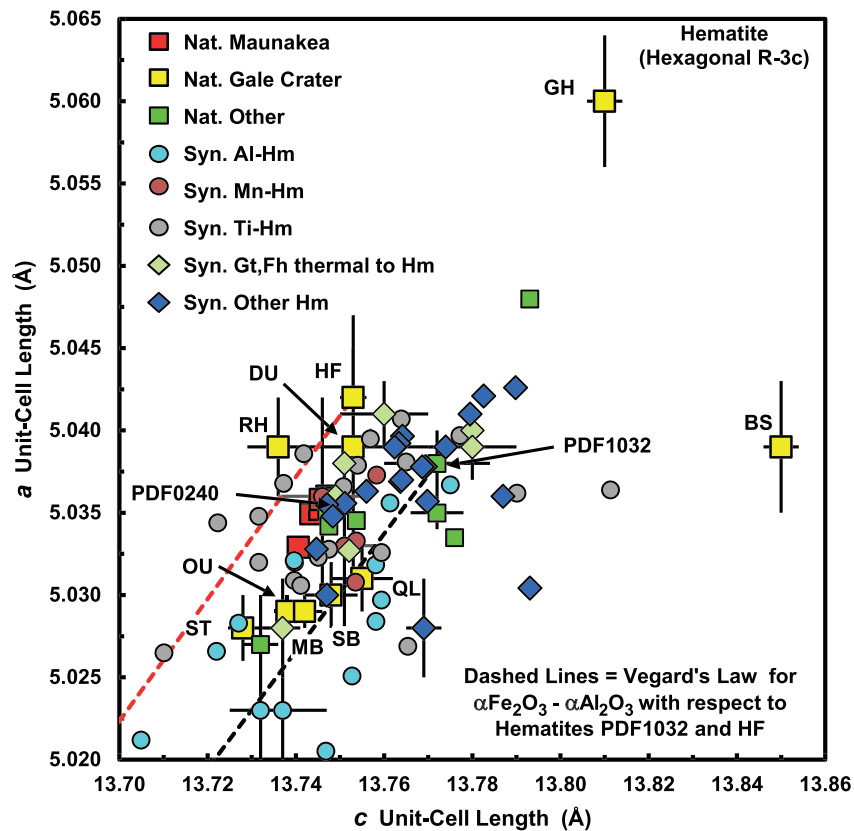


Figure 7. Hematite *c-a* unit-cell plot for Maunakea (red squares), Gale crater drill samples (yellow squares), and literature data for natural (green squares) and synthetic samples. Synthetic samples include Al-substituted hematite (cyan circles), Mn-substituted hematite (rust circles), Ti-substituted hematite (gray circles), hematite from thermal decomposition of goethite and ferrihydrite (light-green diamonds), and various other hematite samples without substitutional impurities (blue diamonds). The black and red dashed lines are Vegard's law calculated between corundum and hematites PDF1032 and HF, respectively (see text). Nat. = natural; Syn. = synthetic; GH = Greenhorn; BS = Big Sky; HF = Highfield; DU = Duluth; RH = Rock Hall; OU = Oudam; QL = Quela; SB = Sabina; MB = Marimba; ST = Stoer; PDF1032 and PDF0204 refer to PDF# 98-000-1032 and PDF# 98-000-0204, respectively.

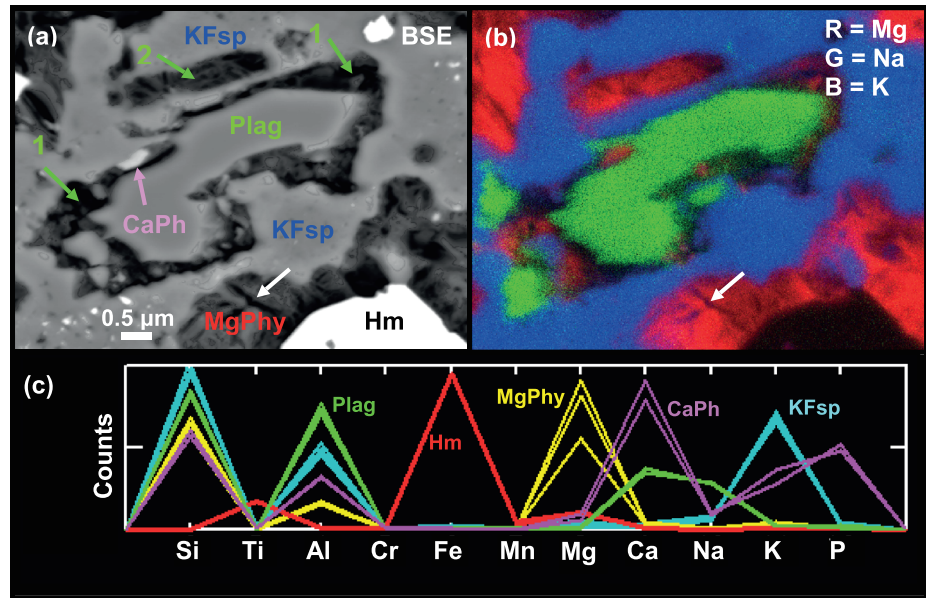


Figure 8. SEM X-ray maps (linear 2% stretch) and element-distribution histogram for a region showing plagioclase dissolution and K-feldspar, hematite, and Mg-phyllsilicate alteration products. (a) BSE image shows void spaces (green arrows) created by complete (#1) and partial (#2) dissolution of plagioclase laths that are partially infilled with a fibrous, (Mg, Si, Al)-rich phase associated with XRD phyllosilicates and EMPA (Mg, Al, Si) composition with a low element total (MgPhy). Note smectite desiccation cracks (white arrows). Ca-phosphate (magenta arrow) and hematite (white) crystals are present. K-feldspar replaces the matrix with crystallite dimensions below the image resolution. (b) RGB image shows spatial distribution of Mg (R), Na (G), and K (B). Void space and compositions (e.g., hematite) having little Mg, Na, and K are black. RGB color purity shows that Mg, Na, and K do not occur together in significant concentrations in any phase. (c) Representative element concentration histograms derived from z axis sampling of the EDX image cube. Plag = plagioclase; KFsp = K-feldspar; MgPhy = Mg-phyllsilicate; Hm = hematite; CaPh = Ca-phosphate.

crystallization/precipitation. (Refer to supporting information for numerical data, literature references, and other sample information.)

3.5. Chemical Dissolution, Precipitation, and Mineral Chemistry and Morphology

SEM images, element maps, and semiquantitative EDX and quantitative EMPA elemental analyses provide information on the spatial distribution and morphology of primary and secondary phases, their chemical compositions, dissolution and other textural changes, and identification of crystalline phases not detected by XRD. Individual SEM BSE and element maps were put into an “element cube” so that a “z axis” profile gives a histogram of relative element concentrations for any selection of map pixels.

In Figure 8 are BSE and red-green-blue (RGB) images and element histograms for a region in HW13MK001 having plagioclase dissolution. Green arrows in the BSE image point to rectangular areas where plagioclase laths were partially (#1) to fully dissolved (#2). The void space is partially infilled by a precipitate having a fibrous morphology, and desiccation cracks, resulting from the vacuum internal to the instrument, are present (white arrows in Figures 8a and 8b). The RGB color purity in Figure 8b shows that Mg, Na, and K do not occur together in significant concentrations in any phase. Void space is black in BSE and RGB images, and nonaluminosilicate compositions having essentially no Mg, Na, and K are white and black in BSE and RGB images, respectively. Coupled with the XRD data discussed above, average EMPA chemistry (Tables 4 and 5), and desiccation cracks, the RGB red (=Mg), green (=Na), and blue (=K) regions, are associated with Mg-phyllsilicate, plagioclase, and sanidine, respectively, and BSE white and RGB black are associated with hematite. The mineralogical assignments are consistent with the element histogram (Figure 8c), and the histogram implies that smectite and, perhaps, 10-Å phyllosilicate are both Mg-based aluminosilicates. A small region having a light gray color (magenta arrow in Figure 8a) corresponds to a Ca-phosphate.

Table 4
Average Mineral Compositions for Weakly Altered Basalt HW13MK021 From EMPA

wt.%	Plag	Ol	TiMt	Matrix
SiO ₂	54.30(64)	36.63(39)	0.10(2)	51.8(28)
TiO ₂	0.15(3)	0.09(2)	17.1(20)	2.8(10)
Al ₂ O ₃	28.25(52)	0.04(1)	5.4(12)	15.8(23)
FeOT	0.78(11)	27.0(17)	67.51(66)	9.8(29)
MnO	0.01(1)	0.64(9)	0.58(12)	nd
MgO	0.08(3)	34.4(16)	4.92(42)	3.1(15)
CaO	10.12(50)	0.29(3)	0.03(3)	6.3(20)
Na ₂ O	5.40(26)	0.03(1)	0.02(2)	5.0(12)
K ₂ O	0.43(9)	0.01(1)	0.01(1)	2.99(76)
Total	99.52(42)	99.20(31)	95.70(46)	97.7(14)
N	49	20	15	10

Note. Numbers in parenthesis are uncertainties of final digit(s) as average standard deviations. Plag = plagioclase; Ol = olivine; TiMt = titanomagnetite. FeOT = total iron as FeO. N = number of analyses.

The plagioclase chemical compositions for relatively unaltered HW13MK021 and the hematite-rich hydrothermally altered samples are the same within error (Tables 4 and 5). Hydrothermally precipitated hematite (by forced hydrolysis) is sourced from dissolution of olivine, Ti-magnetite, and matrix and has subordinate Ti and Mg as nonessential elements. The composition of sanidine (Table 5) approximates stoichiometric KAlSi₃O₈ (SiO₂ = 64.8, Al₂O₃ = 18.3, and K₂O = 16.9, wt.%) with minor Na for K substitution. The Ca-rich phosphate phase was not analyzed by point analysis during EMPA, but the element histogram (Figure 8c) is not consistent with stoichiometric apatite (Ca₅(PO₄)₃F), possibly because the electron beam sampled nearby sanidine.

As discussed above, XRD patterns provide evidence for two phyllosilicates, a smectite with interlayer H₂O and 10-Å phase. The desiccation cracks and element histogram from SEM analysis (Figure 8) and low analysis total by EMPA (~88 wt.%; Table 5) implicate a smectite whose essential elements are Mg, Si, and Al. We were not able to identify, by differences in morphology and chemistry, a separate phase that could be associated with the 10-Å phyllosilicate. If we assume the

Mg-phyllosilicate (MgPhy) composition (Table 5) is the average composition of spatially colocated smectite and 10-Å phases, a conflict is present between this chemistry and that inferred from the XRD data for the 10-Å phase (ferrian mica). Specifically, the mica has Fe and K as essential elements (Hazen et al., 1981), and the measured MgPhy composition (Table 5) has minor contributions from those elements. Similarly, Maunakea smectite is not reasonably interpreted as either nontronite or montmorillonite on the basis of chemistry because the former smectite has Fe and the latter has Ca and Na as essential elements.

MgPhy chemical data are reminiscent of literature data for trioctahedral, Fe-poor smectites. Ballarat and American Canyon saponites have 51.26 and 43.64 wt.% SiO₂, 4.42 and 5.72 wt.% Al₂O₃, 1.14 and 7.27 wt.% Fe₂O₃, 23.54 and 19.35 wt.% MgO, 4.17 and 3.41 wt.% other oxides for 83.09 and 79.39 wt.% totals, respectively, and 4.58 and 1.53 Å for the Ballarat (02ℓ), and (060) reflections, respectively (Post, 1984). Ghassoul (Benhammou et al., 2009) and Kalahari (Mees, 2001) stevensites have 56.5 and 59.71 wt.% SiO₂, 1.31 and 5.18 wt.% Al₂O₃, 24.73 and 14.10 wt.% MgO, 2.63 and 3.89 wt.% other oxides for 85.24 and 82.78 wt.% totals, respectively. The authors report 13.5 and 1.524 Å for Ghassoul (001) and (060) reflections, respectively, and 14.3, 4.51, and 1.529 Å for Kalahari (001), (02ℓ), and (060) reflections, respectively. Additional study is needed to understand the nature of the smectite present in the Maunakea samples, in part because it has excess Al₂O₃ compared to the above trioctahedral smectites.

Table 5
Average Mineral Compositions for Hydrothermally Altered Samples From EMPA

wt.%	Plag	KFsp	MgPhy	Hm	TiMh
SiO ₂	54.1(10)	63.02(28)	45.9(31)	0.04(4)	1.0(11)
TiO ₂	0.14(3)	0.15(13)	0.61(39)	0.10(21)	18.2(37)
Al ₂ O ₃	28.90(50)	19.7(12)	11.6(20)	0.05(7)	6.8(18)
FeOT	0.82(14)	0.67(16)	2.2(12)	88.44(64)	58.0(53)
MnO	0.01(1)	0.03(2)	nd	0.15(19)	1.60(47)
MgO	0.10(6)	0.24(20)	23.4(45)	0.13(15)	5.32(8)
CaO	10.40(60)	0.27(24)	1.6(10)	0.02(4)	0.24(21)
Na ₂ O	5.18(29)	1.65(40)	0.36(40)	0.01(2)	0.24(21)
K ₂ O	0.39(10)	13.33(44)	1.8(23)	0.02(5)	0.12(11)
BaO	0.04(3)	0.06(4)	0.32(24)	0.01(1)	0.06(3)
Total	100.04(88)	99.0(20)	87.8(61)	88.89(36)	90.9(12)
N	37	12	20	30	17

Note. Numbers in parenthesis are the uncertainty of the final digit(s) (standard deviation of average). Plag = plagioclase (andesine); KFsp = potassium feldspar; MgPhy = phyllosilicate; Hm = hematite; TiMh = titanomaghemite. FeOT = total iron as FeO. N = number of analyses.

Figure 9 shows BSE and RGB images and element histograms for a cavity lined with MgPhy (red color in Figure 9b and yellow histogram in Figure 9c) and hematite crystals with well-developed crystal faces (BSE image white, RGB image black, and red histogram). Hematite crystals that were sliced during fabrication of polished sections (red arrows in Figures 9a and 9b) show that they are compositionally zoned (not shown), with the rims enriched in Ti and Mg. Both K-feldspar (blue) and plagioclase laths (green) are present (Figure 9b) as are locations enriched in Ca-phosphate (magenta BSE arrows and element histogram). The BSE image and element histograms also document two unanticipated compositions. The first is a metallic silver particle (BSE white arrow in Figure 9a and element histogram in Figure 9c) that was originally revealed by its high contrast (from high atomic number) in the BSE image. Native Ag particles were uncommon but detected in other polished sections. Less obvious in the BSE image (tan arrow) is a region, sandwiched between MgPhy and a hematite crystal, whose element histogram shows only Ca. Ca-carbonate is implied because the crystal was “burned” by the electron beam.

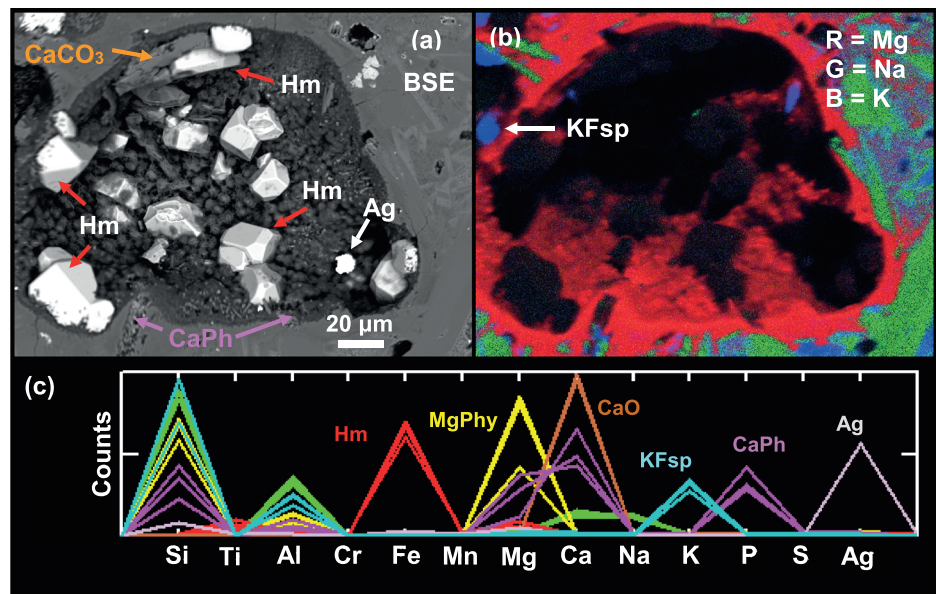


Figure 9. (a and b) SEM X-ray maps (linear 2% stretch) and c representative element distribution histograms for a depression in HW13KM030B lined with precipitated MgPhy (red in b) and polyhedral Hm crystals (bright in a and black in b). Ca-phosphate (partially dissolved; magenta in a) is present as are uncommon occurrences of Ca-carbonate and silver (Ag) metal. The hematite crystals (bright polyhedrons) have well-developed crystal faces. (c) Representative element concentration histograms derived from z axis sampling of the EDX image cube. Plag = plagioclase; KFsp = K-feldspar; MgPhy = Mg-phyllsilicate; Hm = hematite; CaPh = Ca-phosphate; Ag = native silver.

The series of BSE images in Figure 10 document additional spatial relationships among alteration products and residual igneous phases and the size and morphology of alteration products. The image in Figure 10a is typical for many locations. MgPhy precipitate, riddled with desiccation cracks, is rimmed by K-feldspar (KFsp; white arrows). A 10–20 µm hematite crystal is in contact with KFsp and MgPhy. A KFsp region within the white box is shown at higher magnification in Figure 10b. Individual KFsp crystals (confirmed as K + Al + Si by EDX) are acicular in shape (lengths ~1–2 µm and widths <0.5 µm) and form a porous three-dimensional network of overlapping crystals. Their micrometer-scale dimensions are consistent with the observed formation and preservation of high sanidine having a structural state with full Al,Si disorder as discussed above. Hematite plates (~1 µm thick) oriented parallel and perpendicular to the image plane (black arrows) and adjacent to MgPhy are shown in Figure 10c. In one location, polyhedral hematite crystals occur with “leopard spots” (Figure 10d). The spots by EDX are MgPhy, and they extend internal to the hematite crystals, as shown by the crystal that intercepted the polished surface (white circle). The accumulation in a cavity of polyhedral hematite crystals imbedded in MgPhy (Figure 10e) is similar to Figure 9a but without carbonate and native silver. Polyhedral hematite crystals are not always associated with an obvious cavity (Figure 10f). The crystals are thin to thick plates having various orientation with respect to the polished surface. A native silver particle is also present. A massive occurrence of hematite plates oriented parallel and perpendicular to the polished surface is shown in Figure 10g. A general result from SEM imaging is that hematite is predominantly present as isolated crystals and crystal aggregates (often as cement) where individual crystals are larger than ~10 µm in their longest dimension.

Figure 10h is a representative example of the mineralogical/chemical diversity of alteration products that occurs on distance scales of ~250 µm. A large CaCO₃ crystal is present at center of a cavity that is lined and partially filled by MgPhy and has KFsp as its rim. The adjacent cavity (upper right) with a KFsp rim is almost completely filled with MgPhy exhibiting desiccation cracks. Platy hematite crystals (high BSE albedo) are oriented at parallel, perpendicular, and intermediate angles to the surface plane. Rectangular pits (dashed arrows) result from dissolution of preexisting plagioclase laths (phenocrysts). The extreme mineralogical and chemical diversity imaged in Figures 8–10 is a characteristic of nonequilibrium assemblages.

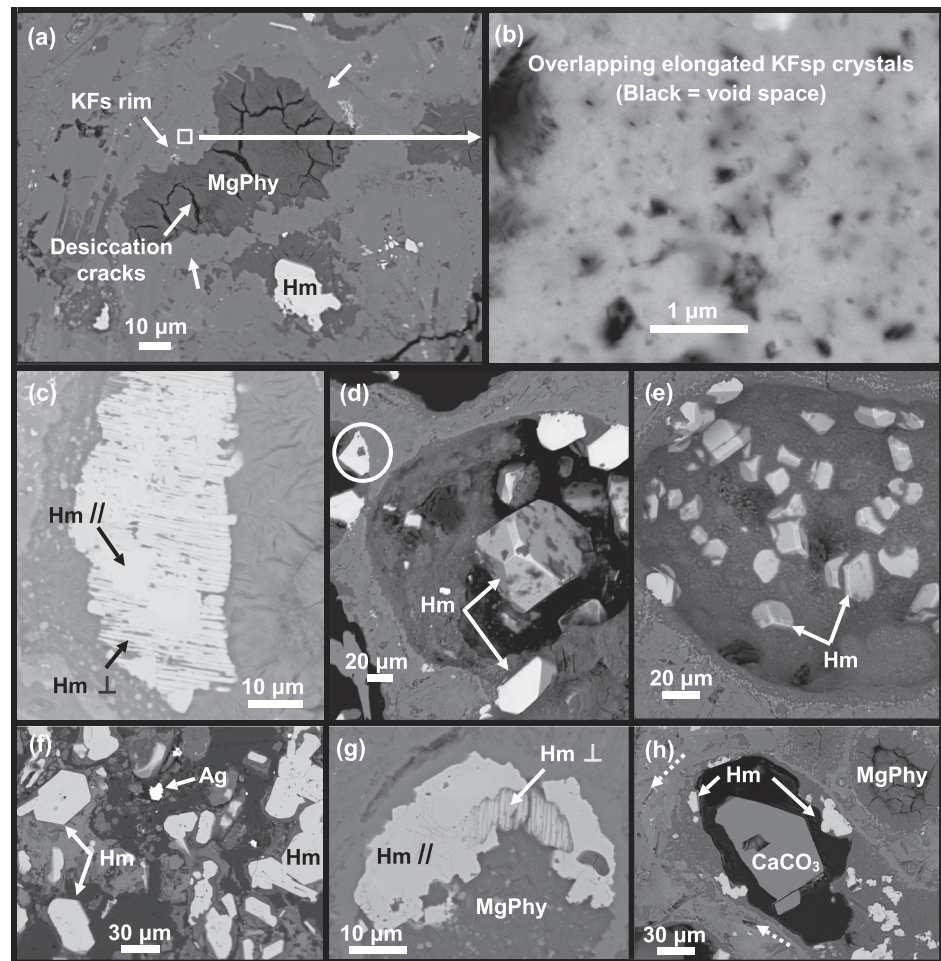


Figure 10. BSE images. (a) Image centered on Mg-phyllsilicate region (with desiccation cracks) and surrounding rim of K-feldspar (arrows). (b) High magnification image of K-feldspar area (square box in a) shows a mush of elongated K-feldspar crystals. (c) Thin Hm plates mostly oriented perpendicular to the surface. (d) Cavity with polyhedral Hm crystals. “Leopard spots” are MgPhy that extends internal to the Hm crystals as shown by sliced Hm crystal (circle). (e) Cavity with polyhedral Hm crystals. (f) Scattered and mostly elongated Hm crystals cut perpendicular to their long axis, showing hexagonal cross sections. High albedo Ag metal particles are present. (g) Accumulation of Hm plates oriented parallel and perpendicular to the surface. (h) CaCO_3 crystal (pseudo-hexagonal habit) in central portion of a cavity rimmed by Hm crystals and MgPhy.

3.6. Specular and Red Hematite

Hematite color at visible wavelengths (~ 380 to 740 nm) is determined by the strength of Fe^{3+} electronic absorption bands. We plot reflectance spectra for red and specular hematite in Figure 11. Two parameters used for spectral identification of red hematite, $S750_500$ (= slope between 500 and 750 nm) and $BD535$ (= band depth at 535 nm relative to a continuum defined by values of reflectance at 500 and 600 nm), are defined in Figure 11a (after Fraeman et al., 2020). Red hematite pigment HMS3 has a mean particle size of $0.14 \mu\text{m}$ (Morris et al., 1985), and specular hematite is the 500–1000 μm sieve fraction of a powder derived by grinding and washing hematite single crystal HMMG1 (Lane et al., 2002). Figure 11b is a plot of $S750_500$ versus $BD535$ for monomineralic powders of red and specular hematite (remeasured Morris et al. [1985] and Lane et al. [2002]) and the 500–1000 and $<150 \mu\text{m}$ size fractions of ground and sieved Maunakea samples. A linear relationship between $S750_500$ and $BD535$ is evident for the monomineralic hematite powders (Figure 11b; dashed line). As anticipated from the gray color of hematite-rich Maunakea samples as hand specimens, their powders plot along the dashed line near the specular hematite end-member as represented by HMMG1 (500–1000 μm).

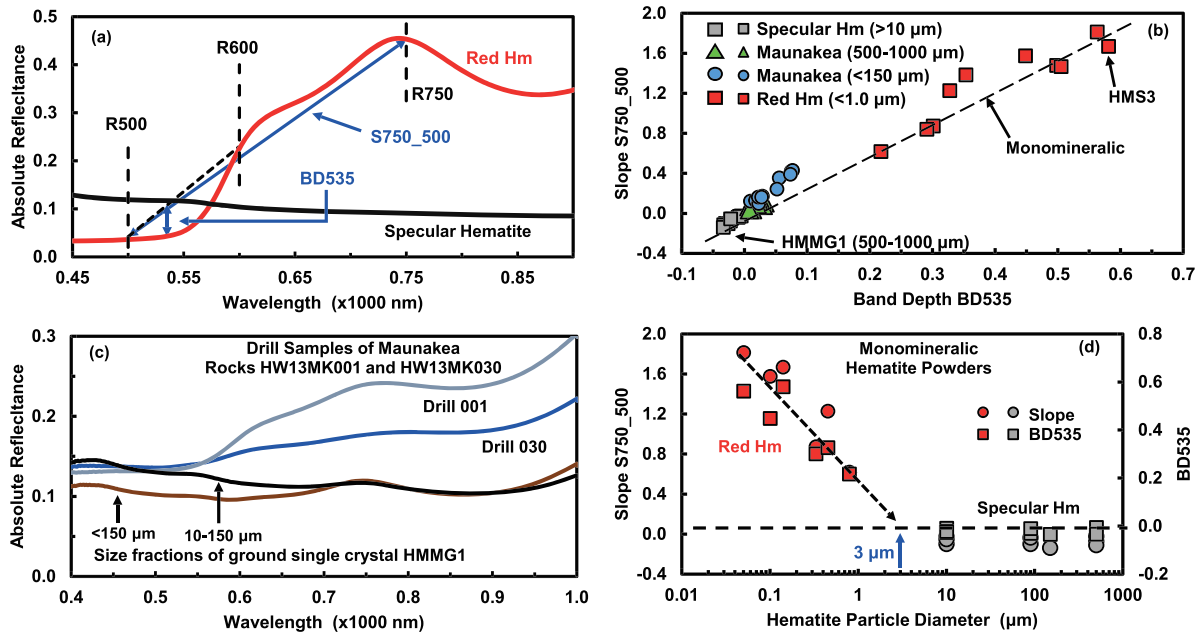


Figure 11. Hematite spectral properties. (a) Reflectance spectra for red hematite HMS3 and specular hematite HMMG1 (500–1000 μm size fraction). Spectral parameters band depth at 535 nm (BD535) and spectral slope between 0.50 and 0.75 μm (S750_500) are defined. (b) Plot of S750_500 versus BD535 for red and specular hematite powders and powders of hydrothermally altered Maunakea rocks. The dashed line is defined by the monomineralic powders. (c) Spectra of drill samples from two Maunakea rocks (HW13MK001 and HW13MK030) compared to those for specular hematite contaminated and not-contaminated by minor red hematite (<150 and 10–150 μm size fractions of HMMG1, respectively). (d) Plot of S750_500 and BD535 versus hematite particle diameter for monomineralic hematite powders. Circle and square symbols are referenced to the slope and band depth axes, respectively; solid red and gray symbols are referenced to red and specular hematite, respectively. Discrete (and single crystal) hematite particles greater than ~3 μm in diameter are specular hematite.

Mechanical abrasion (grinding) of specular hematite does, however, impart red-hematite character to the resulting powders unless the fine particles are removed. This situation is shown in Figure 11c, which has spectra for a <150 μm powder derived by hand-grinding a specular hematite single crystal (HMMG1) and a 10–150 μm powder produced by removing <10 μm particles by sedimentation. Removal of <10 μm particles from the <150 μm powder of HMMG1 resulted in a less red powder by visual observation and by the lower albedo of the <150 μm powder at wavelengths shorter than about 650 nm (Figure 11c).

Figure 11c also has spectra for two powders derived by drilling into different Maunakea rocks (HW13MK001 and HW13MK030) with a MSL-like drill and bit, and their spectral parameters are included in Figure 11b along with those for the <150 and 500–1000 μm size fractions of the Maunakea rocks obtained by grinding and sieving. Setting aside sample-to-sample variations, it is evident that mechanical abrasion introduced a population of fine-grained and red hematite particles that were not initially present and that these particles moved the spectral parameters of the powders toward those for red hematite (i.e., larger values for both S750_500 and BD535). To the eye, the drill and <150 μm powders were dark purple in color.

An imprecise diameter estimate where hematite powders transition from pigmentary (i.e., red) to specular properties is ~3 μm (Figure 11d). For red hematite, mean particle diameters were directly measured (Morris et al., 1985). For specular hematite, minimum size fraction values (e.g., 500 μm for the 500–1000 μm size fraction) from Lane et al. (2002) were used. Catling and Moore (2003) place the transition at 5 μm from hydrothermal processing of aqueous and/or solid Fe³⁺ progenitors at temperatures >100 °C. Both diameter estimates are consistent with Maunakea specular hematite, where the oxide crystals have particle diameters >10 μm as independently measured in SEM images (e.g., Figure 10). Laboratory experiments show, however, that precipitation of red hematite is not precluded at hydrothermal temperatures ≥100 °C (e.g., Ryde & Matijević, 1994; Wang et al., 2005). (Refer to supporting information for hematite spectra between 0.40 and 1.00 μm and derived spectral parameters.)

4. Hydrothermal Environment at Maunakea

We summarize here chemical and mineralogical Maunakea data and literature data to constrain the low-pressure hydrothermal environment that took the presumptive basaltic progenitor (Hawaiitic basalt represented by HW13MK021) to the highly chemically and mineralogically altered samples discussed in this paper. Bulk chemistry and Tau histograms show alteration in an open system with significant mass gain for Fe, Mn, Mg, K, and S ($\text{Tau} > 0$) and significant mass loss for Ca and Na ($\text{Tau} < 0$). The high oxidation state of Fe for altered bulk samples versus progenitor ($\text{Fe}^{3+}/\sum\text{Fe} \sim 1.0$ and ~ 0.4 , respectively) implicates anoxic conditions during progenitor dissolution to facilitate Fe transport as Fe^{2+} and oxic conditions during precipitation of Fe as Fe^{3+} . On the basis of XRD powder patterns, reflectance spectra, and SEM EDX chemistry, specular hematite is the only Fe^{3+} oxide/oxyhydroxide phase detected, and the oxide is only alteration product detected where Fe is present as an essential element. Chemical data imply high-Mg smectite and not nontronite and montmorillonite which have Fe and (Ca,Na) as essential elements, respectively. The unit-cell parameters for the 10-Å phyllosilicate (Table 3) are similar to those for a silica- and alkali-rich ferrian trioctahedral mica (Hazen et al., 1981), but we were not able to confirm the chemical presence of a phase containing K, Mg, and Fe as essential elements after a thorough search with SEM and EMPA element maps and SEM EDX analyses. We speculate that the composition with Si, Mg, and Al as essential elements and a deficit oxide total (MgPhy) corresponds to an average phyllosilicate composition or that the mica was not sampled during our EMPA and SEM chemical analyses.

The observation that Fe was detected as an alteration product predominantly if not solely as Fe^{3+} in specular hematite and not detected in other Fe^{3+} -bearing alteration products including ferrihydrite, goethite, and nontronite implies full Fe precipitation occurred under hydrothermal conditions (forced hydrolysis) at temperatures sufficiently elevated that ferrihydrite, goethite, and other Fe^{3+} bearing phases did not precipitate. The absence of goethite, for example, implies no evidence of an extended period of aqueous alteration at ambient temperatures before the onset of hydrothermal precipitation of specular hematite (Cornell & Schwertmann, 1996). The inferred temperature for hydrothermal precipitation of specular hematite is >100 °C according to the rationale developed by Catling and Moore (2003).

Hydrothermally precipitated Maunakea sanidine (adularia) is characterized by <2 wt.% Na_2O and small crystals with full Al,Si structural disorder. Extreme Al,Si structural disorder for adularia equivalent to the Maunakea occurrence has previously been reported in the literature for natural samples (Figure 6) associated with granitic pegmatites and epithermal (nonalpine) vein deposits (e.g., Černý & Chapman, 1984, 1986; Ferguson et al., 1991). The small crystal size and full structural Al,Si disorder are manifestations of rapid hydrothermal crystallization and rapid descent to low temperatures (thermal quenching) to inhibit Al,Si ordering. Initial hydrothermal temperatures on the order of ~ 150 to ~ 400 °C are inferred for granitic pegmatites and epithermal vein deposits (e.g., Černý and Chapman (1984) citing Nissen (1967); Bethke et al., 2005; Echavarría et al., 2006; Castor et al., 2003; Dreher et al., 1998; Heald et al., 1987). A temperature range between ~ 250 and ~ 400 °C is reasonable for, or is at least not in conflict with, the Maunakea hydrothermal deposit, because it is in excess of the minimum temperature for precipitation of specular hematite (~ 100 °C; Catling & Moore, 2003) and is adequate to inhibit precipitation, and thus the nondetection of phases like ferrihydrite and goethite whose thermal decomposition are near or below ~ 250 °C in dry systems (e.g., Cornell & Schwertmann, 1996; Morris et al., 1985). Interpreted as akin to an epithermal deposit by detections of native silver (Figures 9a and 10f), the Maunakea adularia-hematite deposit is an open-system, volcano-hosted, epithermal deposit in basaltic terrain that underwent rapid cooling to precipitate high sanidine (adularia) having full Al,Si structural disorder and did not experience postprecipitation exposure to order-inducing events.

5. Implications for Gale Crater (Mars)

High sanidine with extreme structural Al,Si disorder was detected in Windjana drill fines by CheMin XRD, and specular hematite was detected in Oudam and Highfield drill fines by CheMin XRD (for mineralogy) and imagery and spectroscopy (for gray color) (Achilles et al., 2020; Rampe et al., 2020; Treiman et al., 2016). Their drill sites along *Curiosity's* traverse are located in Figure 12 (after Grotzinger et al., 2015) along with locations where red hematite was detected in drill samples. By analogy with the Maunakea

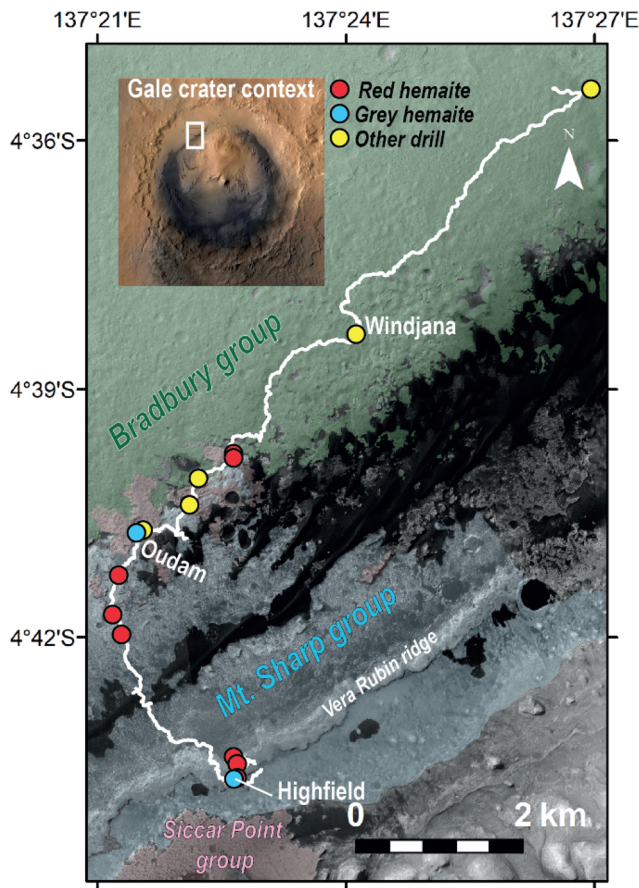


Figure 12. Location of high-sanidine drill sample Windjana, specular hematite drill samples Oudam and Highfield (blue dots), red hematite drill samples (red dots), and drill samples without significant concentrations of crystalline hematite (yellow dots) along *Curiosity's* traverse (white line) on HiRISE orbital image. Locations of stratigraphic groups defined in Grotzinger et al. (2015) are indicated by green (Bradbury group), blue (Mt. Sharp group), and pink (Siccar Point group).

sanidine-hematite hydrothermal deposit, we develop below diagenetic and detrital working hypotheses for these detections.

5.1. High Sanidine

On the *b-c* quadrilateral diagram for alkali feldspars, sanidine for the Windjana drill sample (Morrison et al., 2018) plots proximate to values that correspond to full Al,Si structural disorder (Figures 5b and 6). We restrict discussion of Gale crater samples to Windjana because its unit-cell parameters have the highest precision (error bars are 1σ) (Morrison et al., 2018). As discussed in this paper for a basalt-hosted hydrothermal environment and in the literature for other natural hydrothermal (e.g., Černý & Chapman, 1984, 1986) and pyrogenic environments, the initial formation pathway for sanidine with full Al,Si disorder involves rapid hydrothermal precipitation or rapid cooling as a solid from a fully disordered structural state (~ 1000 °C; e.g., Grove & Hazen, 1974), that is, thermal quenching. For hydrothermal high sanidine, "... it seems likely that the ultimate in K-feldspar disorder occurs exclusively in metastable adularia, grown and preserved in the low temperature stability field of maximum microcline" (Černý & Chapman, 1986). Once formed, fully disordered sanidine must be isolated from order-inducing processes which can accompany diagenesis (e.g., Bermanec et al., 2012; Morad et al., 1989). Maunakea adularia has retained full structural Al,Si disorder since volcanic eruptions ceased (~ 53 ka; Wolfe et al., 1997), and Tanco adularia from a granitic pegmatite (Bernic Lake, Manitoba, CD) has retained full Al,Si structural disorder for ~ 2.6 Ga (Černý & Chapman, 1984). We explored four working hypotheses to explain the presence of high sanidine with full Al,Si structural disorder at Windjana and its stability through geologic time.

1. *Model 1.* Interaction of hydrothermal fluids with local Gale crater basaltic sediment (or sedimentary rock) at ~ 250 to ~ 400 °C, rapid precipitation of high sanidine (adularia) with full Al,Si structural disorder, and no consequential post-precipitation exposure to Al,Si ordering events. This working hypothesis is not accompanied by evidence for a thermal source for hydrothermal activity. The source could be magmatic as at Maunakea or impact melt associated with the Gale impact event (e.g., Achilles et al., 2020; Fraeman et al., 2020; Rampe et al., 2020), with the evidence erased by subsequent geologic processes. The high sanidine is formed in place during diagenesis. Disordered adularia sourced to basaltic (Maunakea volcano; this study) and granitic (Manitoba, Canada) (e.g., Černý & Chapman, 1984; Ferguson et al., 1991) terrains are among terrestrial mineralogical analogues.
2. *Model 2.* Precipitation of high sanidine (adularia) as in *Model 1* at a distant location followed by transport for ultimate incorporation into Windjana sedimentary rock without significant exposure to Al,Si ordering events accompanying transport, lithification, and post-lithification processes. The Windjana high sanidine is detrital.
3. *Model 3.* Crystallization of pyrogenic sanidine (volcanic or impact-melt sourced) and/or reheating (volcanic or impact sourced) of preexisting sanidine with perseveration of high-sanidine structural disorder at a distant location followed by transport for ultimate incorporation into sediment (sedimentary rock) at the Windjana local. A concern here is preservation of extreme Al,Si disorder during cooling from high temperatures. The Al,Si structural disorder for pyrogenic (phenocrystic) sanidines, for example, from the Eifel volcanic field (e.g., Harris et al., 1989, Kimata et al., 1996; Phillips & Ribbe, 1973), is not as extreme as for adularia from Maunakea and Manitoba (Figure 6). However, the initial (but unknown) Al,Si structural state of K-feldspar-bearing granite xenocrysts was reset to extreme Al,Si disorder by reheating to high temperatures (~ 1000 °C; e.g., Grove & Hazen, 1974) by host magmas (Figure 6). At face value, reheating is viable process to accommodate the observed structural state of Windjana high

sanidine, but it is not favorable on a phenomenological basis. The Windjana high sanidine is detrital, irrespective of pyrogenic formation process, and was not significantly exposed to Al,Si ordering events accompanying transport, lithification, and post-lithification processes.

4. *Model 4.* Precipitation of sanidine with extreme Al,Si structural disorder at hydrothermal temperatures and rapid cooling in a meteoritic impact structure followed by transport (including ballistic transport) for ultimate incorporation into Windjana sedimentary rock. The process results in extreme Al,Si structural disorder that is comparable to that observed for adularia described in *Model 1* (Figure 6). A terrestrial analogue is the Lake Lappajairvi impact structure (Finland) (Lehtinen, 1974). The Windjana high sanidine is detrital and was not significantly exposed to Al,Si ordering events accompanying transport, lithification, and postlithification processes.

Diagenetic (*Model 1*) and detrital (*Models 2–4*) models all have, as an essential element, no significant post-formation exposure of Windjana high sanidine to Al,Si ordering events. The detrital models additionally impose no significant exposure of Windjana high-sanidine (and cogenetic material) to Al,Si ordering events during transport and during subsequent lithification. The preferred interpretation of Treiman et al. (2016) and afterward Morrison et al. (2018) is that Windjana high sanidine is detrital in the sedimentary rock and pyrogenic in origin, crystalizing at high temperatures with full Al,Si structural disorder, cooling without significant ordering of the Al,Si structural state, and preservation of the disordered structural state through time. These scenarios are viable, but preservation of extreme Al,Si structural ordering during cooling from pyrogenic temperatures is not a certainty (Figure 6).

The detrital scenarios (*Models 2–4*) do not well explain the dominance of high sanidine over plagioclase in Windjana (26(3) wt.% versus 6(3) wt.%, respectively, with respect to bulk sample; Treiman et al., 2016) under the action of erosional mixing process over significant distances with material whose feldspar is dominated by plagioclase (Figure 5a). This point might be mitigated to some extent by the Confidence Hill drill sample where plagioclase is present with subordinate sanidine (Morrison et al., 2018; Rampe et al., 2017). Alternatively, hydrothermal alteration was present but not as extensive at Confidence Hills.

Our preferred working hypothesis (*Model 1*) for of Windjana sedimentary rock is based primarily on the Maunakea analog: in situ alteration by hydrothermal fluids at ~250–400 °C that results in dissolution of plagioclase, precipitation of diagenetic adularia with full Al,Si structural disorder, and, post precipitation, no significant exposure to order-inducing geologic events. A thermal source for hydrothermal activity is not evident, but the possibility of diagenetic hydrothermal sanidine at Windjana adds to recent hypotheses for elevated temperatures elsewhere within Gale crater to explain detections of tridymite (Yen, Morris, et al., 2017) and, as discussed next, specular hematite (Achilles et al., 2020; Fraeman et al., 2020; Rampe et al., 2020). Evidence for thermal sources could have been obscured/erased by geologic events occurring after cessation of hydrothermal activity.

5.2. Specular and Red Hematite

The MSL CheMin instrument detected crystalline hematite to various extents in drill samples from Mt. Sharp (Achilles et al., 2020; Morrison et al., 2018; Rampe et al., 2017, 2020). Specular, as opposed to red, hematite is potential evidence for hydrothermal precipitation of hematite at temperatures >100 °C (Catling & Moore, 2003). Both specular hematite (Maunakea samples; $a = 5.035(1)$ Å and $c = 13.746(2)$ Å from Table 2) and red hematite (e.g., red ochre samples; $a = 5.036(4)$ Å and $c = 13.741(46)$ Å from supporting information) have the same average unit-cell lengths by Rietveld refinement within uncertainty (also see Figure 7), showing that unit-cell lengths do not reliably differentiate between specular and red hematite. The relatively flat spectral slope of specular hematite (BD535~0) and its low albedo at visible wavelengths strongly contrasts with the corresponding behavior for red hematite (positive spectral spectra slope and BD535 > 0.2) (Figure 11), providing a way to access the relative spectral proportions of specular and red hematite in drill tailings on the basis of spectroscopy and color imagery and in the absence significant proportions other black pigments like magnetite.

From true-color images and spectroscopy of drill tailings and nearby surface, specular hematite and therefore potential hydrothermal activity is indicated for Oudam and Highfield drill samples from the lower slope and VRR of Mt. Sharp, respectively (Achilles et al., 2020; Rampe et al., 2020). With respect to color, VRR can be characterized in general as relatively red in color (interpreted as red hematite) with

scattered gray patches ~10 m in diameter (interpreted as specular hematite) (Fraeman et al., 2020). Following the color, hydrothermal precipitation of specular hematite is indicated for the gray patches, but hydrothermal conditions are neither implied nor excluded for precipitation of red hematite in VRR relatively red areas. The presence of high sanidine with full Al,Si structural disorder in the Kimberly formation (Windjana drill sample) but not at Oudam and VRR may reflect the relative availability of potassium in hydrothermal fluids.

Except for Greenhorn and Big Sky, hematite unit-cell lengths for drill samples plot within (Stoer, Oudam, Marimba, Sebina, Quela, and Duluth) or proximate to (Rock Hall and Highfield) the range of values observed for terrestrial and synthetic samples whose hematite unit-cell lengths are not influenced by Al, Mn, and Ti substitutional cations (Figure 7). Thus, those elements need not be specifically implicated to explain the range of unit-cell lengths for Gale hematite. The implication is contrary to terrestrial experience where Al-substitution in ferric oxides and oxyhydroxides as products of alteration and weathering is well documented (e.g., Cornell & Schwertmann, 1996; Stanjek & Schwertmann, 1992). However, we have insufficient information from *Curiosity's* instruments to use as robust evidence for or against Al-bearing hematite in any drill sample. Because Al for Fe substitution in hematite results in lower values for *a* and *c* unit-cell lengths relative to its unsubstituted equivalent (Figure 7), Rampe et al. (2020) speculate on this basis that hematite unit-cell parameters for Stoer could be influenced by Al substitution.

Acknowledgments

Maunakea field work and samples were obtained in partnership with the Pacific International Space Center for Exploration Systems with permission from the Office of Mauna Kea Management, the Mauna Kea Management Board, Board of Land and Natural Resources, and the cultural Hawaiian Kahu Kū Mauna Council. We are greatly appreciative of the shared knowledge and sustained efforts of these organizations in the protection and preservation of the unique cultural and natural resources of Maunakea. The manuscript benefitted from careful reading and comments by anonymous reviewers and from discussion with John Grotzinger. Supporting Information consists of two spreadsheets available for downloading from the Open Data Repository (<https://odr.io/> Morrisetal2020_JGR_2019JE006324): (a) direct download of unit-cell parameters for sanidine and hematite (<https://odr.io/view/downloadfile/60903>) and (b) direct download of hematite spectra and spectral parameters (<https://odr.io/view/downloadfile/60902>) and direct download of Maunakea XRD patterns (<https://odr.io/view/downloadfile/60904>). Support for this work by the NASA Mars Science Laboratory Project, the NASA Johnson Space Center, and the Jet Propulsion Laboratory, California Institute of Technology (under a contract with NASA) is acknowledged.

References

- Abad-Ortega, M. M., Fenoll Hach-Ali, P., Martin-Ramos, J. D., & Ortega-Huertas, M. (1993). The feldspars of the Sierra Albarrana granitic pegmatites, Cordoba, Spain. *Canadian Mineralogist*, *33*, 185–202.
- Achilles, C. N., Rampe, E. B., Downs, R. T., Bristow, T. F., Ming, D. W., Morris, R. V., et al. (2020). Evidence for multiple diagenetic episodes in ancient fluvial-lacustrine sedimentary rocks in Gale Crater, Mars. *Journal of Geophysical Research: Planets*, *125*, e2019JE006295. <https://doi.org/10.1029/2019JE006295>
- Alvarez, M., Rueda, E. H., & Sileo, E. E. (2006). Structural characterization and chemical reactivity of synthetic Mn-goethites and hematites. *Chemical Geology*, *231*(4), 288–299. <https://doi.org/10.1016/j.chemgeo.2006.02.003>
- Anderson, S. P., Dietrich, W. E., & Brimhall, G. H. Jr. (2002). Weathering profiles, mass-balance analysis, and rates of solute loss: Linkages between weathering and erosion in a small, steep catchment. *Geological Society of America Bulletin*, *114*(9), 1143–1158.
- Angel, R., Hazen, R., McCormick, T., Prewitt, C., & Smyth, J. (1988). Comparative compressibility of end-member feldspars. *Physics and Chemistry of Minerals*, *15*(4), 313–318. <https://doi.org/10.1007/BF00311034>
- Benhammou, A., Tanouti, B., Nibou, L., Yaacoubi, A., & Bonnet, J.-P. (2009). Mineralogical and physicochemical investigation of Mg-smectite from Jbel Ghassoul, Morocco. *Clays and Clay Minerals*, *57*(2), 264–270. <https://doi.org/10.1346/CCMN.2009.0570212>
- Berger, J. A., Schmidt, M. E., Campbell, J. L., Flannigan, E. L., Gellert, R., Ming, W., & Morris, R. V. (2020). Particle induced X-ray Emission spectrometry (PIXE) of Hawaiian volcanics: An analogue study to evaluate the APXS field analysis of geologic materials on Mars. *Icarus*, *113*708.
- Bermanec, V., Horvat, M., Žigovčič Gobac, Ž., Zebec, V., Scholz, R., Škoda, R., et al. (2012). Pseudomorphs of low microcline after adularia fourlings from the Alto da Cabeça (Boqueirão) and Morro Redondo pegmatites, Brazil. *The Canadian Mineralogist*, *50*(4), 975–987. <https://doi.org/10.3749/canmin.50.4.975>
- Bethke, P. M., Rye, R. O., Stoffregen, R. E., & Vikre, P. G. (2005). Evolution of the magmatic-hydrothermal acid-sulfate system at Summitville, Colorado: Integration of geological, stable-isotope, and fluid-inclusion evidence. *Chemical Geology*, *215*(1–4), 281–315. <https://doi.org/10.1016/j.chemgeo.2004.06.041>
- Blake, D., Vaniman, D., Achilles, C., Anderson, R., Bish, D., Bristow, T., et al. (2012). Characterization and calibration of the CheMin mineralogical instrument on Mars Science Laboratory. *Space Science Reviews*, *170*(1–4), 341–399. <https://doi.org/10.1007/s11214-012-9905-1>
- Blake, R., Hessevick, R., Zoltai, T., & Finger, L. W. (1966). Refinement of the hematite structure. *American Mineralogist: Journal of Earth and Planetary Materials*, *51*(1–2), 123–129.
- Blasi, A., Brajkovic, A., & Blasi, C. D. P. (1982). Highly ordered monoclinic K-feldspars from Haut Boréon anatectites, Argentera Massif, Maritime Alps. *Tschermaks Mineralogische Und Petrographische Mitteilungen*, *29*(4), 241–253. <https://doi.org/10.1007/BF01091795>
- Boyd, F. R., & Mertzman, S. A. (1987). Composition and structure of the Kaapvaal lithosphere, southern Africa. *Magmatic processes: Physicochemical principles, spec. publ. geochem. soc.* (Vol. 1, pp. 13–24). The Geochemical Society.
- Brimhall, G. H., & Dietrich, W. E. (1987). Constitutive mass balance relations between chemical composition, volume, density, porosity, and strain in metasomatic hydrochemical systems: Results on weathering and pedogenesis. *Geochimica et Cosmochimica Acta*, *51*(3), 567–587. [https://doi.org/10.1016/0016-7037\(87\)90070-6](https://doi.org/10.1016/0016-7037(87)90070-6)
- Bristow, T. F., Rampe, E. B., Achilles, C. N., Blake, D. F., Chipera, S. J., Craig, P., et al. (2018). Clay mineral diversity and abundance in sedimentary rocks of Gale Crater, Mars. *Science Advances*, *4*(6), eaar3330. <https://doi.org/10.1126/sciadv.aar3330>
- Castor, S. B., Boden, D. R., Henry, C. D., Cline, J. S., Hofstra, A. H., McIntosh, W. C., et al. (2003). The Tuscarora Au-Ag district: Eocene volcanic-hosted epithermal deposits in the Carlin gold region, Nevada. *Economic Geology*, *98*(2), 339–366.
- Catling, D. C., & Moore, J. M. (2003). The nature of coarse-grained crystalline hematite and its implications for the early environment of Mars. *Icarus*, *165*(2), 277–300. [https://doi.org/10.1016/S0019-1035\(03\)00173-8](https://doi.org/10.1016/S0019-1035(03)00173-8)
- Černý, P., & Chapman, R. (1984). Paragenesis, chemistry and structural state of adularia from granitic pegmatites. *Bulletin de Mineralogie*, *107*(3), 369–384. <https://doi.org/10.3406/bulmi.1984.7767>
- Černý, P., & Chapman, R. (1986). Adularia from hydrothermal vein deposits; extremes in structural state. *The Canadian Mineralogist*, *24*(4), 717–728.

- Černý, P., Galliski, M. A., Oyarzábal, J. C., Teertstra, D. K., Chapman, R., MacBride, L., & Ferreira, K. (2003). Stranded and equilibrated assemblages of late feldspars in two granitic pegmatites in the Pampean ranges, Argentina. *The Canadian Mineralogist*, *41*(4), 1013–1026. <https://doi.org/10.2113/gscanmin.41.4.1013>
- Cherry, M. E., & Trembath, L. T. (1978). Structural state and composition of alkali feldspars in granites of the St. George pluton, southwestern New Brunswick. *Mineralogical Magazine*, *42*(323), 391–399.
- Collerson, K. (1976). Composition and structural state of alkali feldspars from high-grade metamorphic rocks, central Australia. *American Mineralogist*, *61*(3–4), 200–211.
- Colville, A. A., & Ribbe, P. H. (1968). The crystal structure of an adularia and a refinement of the structure of orthoclase. *American Mineralogist: Journal of Earth and Planetary Materials*, *53*(1–2), 25–37.
- Cornell, R., & Schwertmann, U. (1996). *The Iron Oxides: Structure, Properties, Reactions, Occurrences, and Uses* (p. 573). New York: VHC.
- da Cunha, C. C., & da Costa, G. M. (2016). Water determination in iron oxyhydroxides and iron ores by Karl Fischer titration. *Physics and Chemistry of Minerals*, *43*(10), 739–748. <https://doi.org/10.1007/s00269-016-0830-9>
- Das, S., & Hendry, M. J. (2014). Characterization of hematite nanoparticles synthesized via two different pathways. *Journal of Nanoparticle Research*, *16*(8), 2535. <https://doi.org/10.1007/s11051-014-2535-7>
- Denton, A. R., & Ashcroft, N. W. (1991). Vegard's law. *Physical Review A*, *43*(6), 3161–3164. <https://doi.org/10.1103/PhysRevA.43.3161>
- Deubener, J., Sternitzke, M., & Mueller, G. (1991). Feldspars MAlSi_3O_8 (M = H, Li, Ag) synthesized by low-temperature ion exchange. *American Mineralogist*, *76*(9–10), 1620–1627.
- Dong, G., & Morrison, G. (1995). Adularia in epithermal veins, Queensland: Morphology, structural state and origin. *Mineralium Deposita*, *30*(1), 11–19.
- Dreher, A. M., Vlach, S. R. F., & Martini, S. L. (1998). Adularia associated with epithermal gold veins in the Tapajós Mineral Provinces, Pará State, Northern Brazil. *Revista Brasileira de Geociências*, *28*(3), 397–404. <https://doi.org/10.25249/0375-7536.1998397404>
- Echavarría, L., Nelson, E., Humphrey, J., Chavez, J., Escobedo, L., & Iriando, A. (2006). Geologic evolution of the Caylloma epithermal vein district, southern Peru. *Economic Geology*, *101*(4), 843–863. <https://doi.org/10.2113/gsecongeo.101.4.843>
- Emerson, R., & Guidotti, C. V. (1974). New X-ray and chemical data on C. G. Hewlett's Feldspar Suite. *American Mineralogist: Journal of Earth and Planetary Materials*, *59*(5–6), 615–617.
- Ferguson, R. B., Ball, N. A., & Černý, P. (1991). Structure refinement of an adularian end-member high sanidine from the Buck Claim pegmatite, Bernic Lake, Manitoba. *The Canadian Mineralogist*, *29*(3), 543–552.
- Fitz Gerald, J. D., Parise, J. B., & MacKinnon, I. D. (1986). Average structure of an An_{48} plagioclase from the Hogarth Ranges. *American Mineralogist*, *71*(11–12), 1399–1408.
- Fox, P. E., & Moore, J. M. Jr. (1969). Feldspars from Adamant pluton, British Columbia. *Canadian Journal of Earth Sciences*, *6*(5), 1199–1209. <https://doi.org/10.1139/e69-121>
- Fraeman, A. A., Johnson, J. R., Arvidson, R. E., Rice, M. S., Wellington, D. F., Morris, R. V., et al. (2020). Synergistic ground and orbital observations of iron oxides on Mt. Sharp and Vera Rubin Ridge. *Journal of Geophysical Research: Planets*, *125*, e2019JE006294. <https://doi.org/10.1029/2019JE006294>
- Gilbert, B., Frandsen, C., Maxey, E., & Sherman, D. (2009). Band-gap measurements of bulk and nanoscale hematite by soft X-ray spectroscopy. *Physical Review B*, *79*(3), 035108. <https://doi.org/10.1103/PhysRevB.79.035108>
- Gladney, E. S., O'Malley, B. T., Roelandts, I., & Gills, T. E. (1987). *NBS Special Publication 260–111*. Washington DC: US Department of Commerce.
- Glazner, A. F. (1988). Stratigraphy, structure, and potassic alteration of Miocene volcanic rocks in the Sleeping Beauty area, central Mojave Desert, California. *Geological Society of America Bulletin*, *100*(3), 424–435. [https://doi.org/10.1130/0016-7606\(1988\)100<0424:SSAPAO>2.3.CO;2](https://doi.org/10.1130/0016-7606(1988)100<0424:SSAPAO>2.3.CO;2)
- Golden, D. C., Morris, R. V., Lauer, H. V. Jr., & Yang, S. R. (1993). Mineralogy of three slightly palagonitized tephra samples from the summit of Maunakea, Hawaii. *Journal of Geophysical Research*, *98*(E2), 3401–3411. <https://doi.org/10.1029/92JE02590>
- Goss, C. (1987). The kinetics and reaction mechanism of the goethite to hematite transformation. *Mineralogical Magazine*, *51*(361), 437–451. <https://doi.org/10.1180/minmag.1987.051.361.11>
- Grew, E. S. (1979). Al-Si disorder of K-feldspar in crustal xenoliths at Kilbourne Hole, New Mexico. *American Mineralogist*, *64*, 912–916.
- Grotzinger, J., Gupta, S., Malin, M., Rubin, D., Schieber, J., Siebach, K., et al. (2015). Deposition, exhumation, and paleoclimate of an ancient lake deposit, Gale Crater, Mars. *Science*, *350*(6257), aac7575.
- Grotzinger, J. P., Crisp, J., Vasavada, A. R., Anderson, R. C., Baker, C. J., Barry, R., et al. (2012). Mars Science Laboratory mission and science investigation. *Space Science Reviews*, *170*(1–4), 5–56. <https://doi.org/10.1007/s11214-012-9892-2>
- Grove, T. L., & Hazen, R. M. (1974). Alkali feldspar unit-cell parameters at liquid nitrogen temperature: Low temperature limits of the displacive transformation. *American Mineralogist: Journal of Earth and Planetary Materials*, *59*(11–12), 1327–1329.
- Guidotti, C. V., Herd, H., & Tuttle, C. (1973). Composition and structural state of K-feldspars from K-feldspar+ sillimanite grade rocks in Northwestern Maine. *American Mineralogist: Journal of Earth and Planetary Materials*, *58*(7–8), 705–716.
- Guinness, E. A., Arvidson, R. E., Jolliff, B. J., Seelos, K. D., Seelos, F. P., Ming, D. W., et al. (2007). Hyperspectral reflectance mapping of cinder cones at the summit of Mauna Kea and implications for equivalent observations on Mars. *Journal of Geophysical Research*, *112*, E08S11. <https://doi.org/10.1029/2006JE002822>
- Hamilton, V. E., Morris, R. V., Gruener, J. E., & Mertzman, S. A. (2008). Visible, near infrared, and middle infrared spectroscopy of altered basaltic tephra: Spectral signatures of phyllosilicates, sulfates, and other aqueous alteration products with application to the Columbia Hills of Gusev crater, Mars. *Journal of Geophysical Research*, *113*, E12S43. <https://doi.org/10.1029/2007JE003049>
- Harris, M. J., Salje, E. K., Guttler, B. K., & Carpenter, M. A. (1989). Structural states of natural potassium feldspar: An infrared spectroscopic study. *Physics and Chemistry of Minerals*, *16*(7), 649–658.
- Hazen, R., Finger, L., & Velde, D. (1981). Crystal structure of a silica-and alkali-rich trioctahedral mica. *American Mineralogist*, *66*(5–6), 586–591.
- Heald, P., Foley, N. K., & Hayba, D. O. (1987). Comparative anatomy of volcanic-hosted epithermal deposits; acid-sulfate and adularia-sericite types. *Economic Geology*, *82*(1), 1–26. <https://doi.org/10.2113/gsecongeo.82.1.1>
- Hewlett, C. (1959). Optical properties of potassic feldspars. *Geological Society of America Bulletin*, *70*(5), 511–538. [https://doi.org/10.1130/0016-7606\(1959\)70\[511:OPOPF\]2.0.CO;2](https://doi.org/10.1130/0016-7606(1959)70[511:OPOPF]2.0.CO;2)
- Horgan, B., Fraeman, A., Johnson, J. R., Thompson, L., Jacob, S., Bell, J. F. III, & Grotzinger, J. (2019). Redox conditions during diagenesis in the Vera Rubin Ridge, Gale Crater, Mars, from Mastcam multispectral images. 50th Lunar and Planetary Science Conference, The Woodlands, TX. <https://www.hou.usra.edu/meetings/lpsc2019/pdf/1424.pdf>

- Jercher, M., Pring, A., Jones, P. G., & Raven, M. D. (1998). Rietveld X-ray diffraction and X-ray fluorescence analysis of Australian aboriginal ochres. *Archaeometry*, 40(2), 383–401. <https://doi.org/10.1111/j.1475-4754.1998.tb00845.x>
- Kallaste, T. (2014). *Pyroclastic Sanidine in the Lower Palaeozoic Bentonites—A Tool for Regional Geological Correlations* (p. 33). Tallinn, Estonia: Tallinn University of Technology.
- Kimata, M., Shimizu, M., & Saito, S. (1996). High-temperature crystal structure of sanidine. Part II. The crystal structure of sanidine at 935 °C. *European Journal of Mineralogy*, 15-2.
- Kniess, C. T., Cardoso de Lima, J., & Prates, P. B. (2012). The quantification of crystalline phases in materials: Applications of Rietveld method. *Sintering-Methods and Products*, 293–316.
- Kroll, H., & Ribbe, P. H. (1987). Determining (Al,Si) distribution and strain in alkali feldspars using lattice parameters and diffraction-peak positions; a review. *American Mineralogist*, 72(5–6), 491–506.
- Lane, M. D., Morris, R. V., Mertzman, S. A., & Christensen, P. R. (2002). Evidence for platy hematite grains in Sinus Meridiani, Mars. *Journal of Geophysical Research*, 107(E12), 5126. <https://doi.org/10.1029/2001JE001832>
- Lehtinen, M. (1974). Degree of Al/Si order in potassium feldspars. A combination of X-ray and infrared data. *Contributions to Mineralogy and Petrology*, 47(3), 223–230.
- Lehtinen, M., & Sahama, T. G. (1981). A note on the feldspars in the granite xenoliths of the nyiragongo magma. *Bulletin Volcanologique*, 44(3), 451–454. <https://doi.org/10.1007/BF02600576>
- Lemine, O., Sajieddine, M., Bououdina, M., Msalam, R., Mufti, S., & Alyamani, A. (2010). Rietveld analysis and Mössbauer spectroscopy studies of nanocrystalline hematite α -Fe₂O₃. *Journal of Alloys and Compounds*, 502(2), 279–282. <https://doi.org/10.1016/j.jallcom.2010.04.175>
- Li, W., Liang, X., An, P., Feng, X., Tan, W., Qiu, G., et al. (2016). Mechanisms on the morphology variation of hematite crystals by Al substitution: The modification of Fe and O reticular densities. *Scientific Reports*, 6(1), 35,960. <https://doi.org/10.1038/srep35960>
- Majzlan, J., Navrotsky, A., & Evans, B. (2002). Thermodynamics and crystal chemistry of the hematite–corundum solid solution and the FeAlO₃ phase. *Physics and Chemistry of Minerals*, 29(8), 515–526. <https://doi.org/10.1007/s00269-002-0261-7>
- Malik, V., Sen, S., Gelting, D. R., Gajdardziska-Josifovska, M., Schmidt, M., & Guptasarma, P. (2014). Field-enhanced magnetic moment in ellipsoidal nano-hematite. *Materials Research Express*, 1(2), 026114. <https://doi.org/10.1088/2053-1591/1/2/026114>
- Maslen, E., Streltsov, V., Streltsova, N., & Ishizawa, N. (1994). Synchrotron X-ray study of the electron density in α -Fe₂O₃. *Acta Crystallographica Section B: Structural Science*, 50(4), 435–441. <https://doi.org/10.1107/S0108768194002284>
- Mees, F. (2001). An occurrence of lacustrine Mg-smectite in a pan of the southwestern Kalahari, Namibia. *Clay Minerals*, 36(4), 547–556.
- Menna, M., Tribaudino, M., & Renzulli, A. (2008). Al-Si order and spinodal decomposition texture of a sanidine from igneous clasts of Stromboli (southern Italy): Insights into the timing between the emplacement of a shallow basic sheet intrusion and the eruption of related ejecta. *European Journal of Mineralogy*, 20(2), 183–190. <https://doi.org/10.1127/0935-1221/2008/0020-1795>
- Morad, S., Márfil, R., & De La Pena, J. A. (1989). Diagenetic K-feldspar pseudomorphs in the Triassic Buntsandstein sandstones of the Iberian range, Spain. *Sedimentology*, 36(4), 635–650. <https://doi.org/10.1111/j.1365-3091.1989.tb02090.x>
- Morris, R. V., Golden, D. C., Bell, J. F. III, Shelfer, T. D., Scheinost, A. C., Hinman, N. W., et al. (2000). Mineralogy, composition, and alteration of Mars Pathfinder rocks and soils: Evidence from multispectral, elemental, and magnetic data on terrestrial analogue, SNC meteorite, and Pathfinder samples. *Journal of Geophysical Research*, 105, 1757–1817. <https://doi.org/10.1029/1999JE001059>
- Morris, R. V., Lauer, H. V. Jr., Lawson, C., Gibson, A. E. Jr., Nace, K. G., & Stewart, C. (1985). Spectral and other physicochemical properties of submicron powders of hematite (α -Fe₂O₃), maghemite (γ -Fe₂O₃), magnetite (Fe₃O₄), goethite (α -FeOOH), and lepidocrocite (γ -FeOOH). *Journal of Geophysical Research*, 90(B4), 3126–3144. <https://doi.org/10.1029/JB090iB04p03126>
- Morris, R. V., Ming, D. W., Golden, D. C., & Bell, J. F. III (1996). An occurrence of jarositic tephra on Mauna Kea, Hawaii: Implications for the ferric mineralogy of the Martian surface. In M. D. Dyar, C. McCammon, & M. W. Schaefer (Eds.), *Mineral Spectroscopy: A tribute to Roger G. Burns* (pp. 327–336). Houston: The Geochemical Society, Special Publication No. 5.
- Morris, R. V., Ming, D. W., Graff, T. G., Arvidson, R. E., Bell, J. F. III, Squyres, S., et al. (2005). Hematite spherules in basaltic tephra altered under aqueous, acid-sulfate conditions on Maunakea volcano, Hawaii: Possible clues for the occurrence of hematite-rich spherules in the Burns formation at Meridiani Planum, Mars. *Earth and Planetary Science Letters*, 240, 168–178.
- Morrison, S. M., Downs, R. T., Blake, D. F., Vaniman, D. T., Ming, D. W., Hazen, R. M., et al. (2018). Crystal chemistry of Martian minerals from Bradbury Landing through Naukluff Plateau, Gale crater, Mars. *American Mineralogist*, 103(6), 857–871. <https://doi.org/10.2138/am-2018-6124>
- Neusser, G., Abart, R., Fischer, F., Harlov, D., & Norberg, N. (2012). Experimental Na/K exchange between alkali feldspar and an NaCl–KCl salt melt: Chemically induced fracturing and element partitioning. *Contributions to Mineralogy and Petrology*, 164(2), 341–358. <https://doi.org/10.1007/s00410-012-0741-9>
- Nissen, H.-U. (1967). Adular aus den Schweizeralpen: Domänengefüge, Natriumgehalt, Natriumentmischung und Gitterkonstanten. *Schweizerische Mineralogische und Petrographische Mitteilungen*, 47, 1140–1145.
- Norberg, N., Harlov, D., Neusser, G., Wirth, R., & Rhede, D. (2014). Element mobilization during feldspar metasomatism: An experimental study. *European Journal of Mineralogy*, 26(1), 71–82. <https://doi.org/10.1127/0935-1221/2013/0025-2342>
- Orville, P. M. (1967). Unit-cell parameters of the microcline-low albite and the sanidine-high albite solid solution series. *American Mineralogist: Journal of Earth and Planetary Materials*, 52(1–2), 55–86.
- Osinski, G. R. (2004). Impact melt rocks from the Ries structure, Germany: An origin as impact melt flows? *Earth and Planetary Science Letters*, 226(3–4), 529–543. <https://doi.org/10.1016/j.epsl.2004.08.012>
- Parsons, I., Fitz Gerald, J. D., & Lee, M. R. (2015). Routine characterization and interpretation of complex alkali feldspar intergrowths. *American Mineralogist*, 100(5–6), 1277–1303. <https://doi.org/10.2138/am-2015-5094>
- Phillips, M. W., & Ribbe, P. H. (1973). The structures of monoclinic potassium-rich feldspars. *American Mineralogist: Journal of Earth and Planetary Materials*, 58(3–4_Part_1), 263–270.
- Post, J. L. (1984). Saponite from near Ballarat, California. *Clays and Clay Minerals*, 32(2), 147–153. <https://doi.org/10.1346/CCMN.1984.0320209>
- Rampe, E. B., Bristow, T. F., Morris, R. V., Morrison, S. M., Achilles, C. N., Ming, D. W., et al. (2020). Mineralogy of Vera Rubin Ridge from the Mars Science Laboratory CheMin Instrument. *Journal of Geophysical Research: Planets*, 125, e2019JE006306. <https://doi.org/10.1029/2019JE006306>
- Rampe, E. B., Ming, D. W., Blake, D. F., Bristow, T. F., Chipera, S. J., Grotzinger, J. P., et al. (2017). Mineralogy of an ancient lacustrine mudstone succession from the Murray formation, Gale crater, Mars. *Earth and Planetary Science Letters*, 471, 172–185. <https://doi.org/10.1016/j.epsl.2017.04.021>

- Reichen, L. E., & Fahey, J. J. (1962). An improved method for the determination of FeO in rocks and minerals including garnet. *U.S. Geological Survey Bulletin*, 1144B, 1–5.
- Reufer, M., Dietsch, H., Gasser, U., Grobety, B., Hirt, A., Malik, V. K., & Schurtenberger, P. (2011). Magnetic properties of silica coated spindle-type hematite particles. *Journal of Physics: Condensed Matter*, 23(6), 065102. <https://doi.org/10.1088/0953-8984/23/6/065102>
- Ruan, H., & Gilkes, R. (1995). Acid dissolution of synthetic aluminous goethite before and after transformation to hematite by heating. *Clay Minerals*, 30(1), 55–65. <https://doi.org/10.1180/claymin.1995.030.1.06>
- Ryde, N. P., & Matijević, E. (1994). Color effects of uniform colloidal particles of different morphologies packed into films. *Applied Optics*, 33(31), 7275–7281. <https://doi.org/10.1364/AO.33.007275>
- Scambos, T. A., Smyth, J. R., & McCormick, T. C. (1987). Crystal-structure refinement of high sanidine from the upper mantle. *American Mineralogist*, 72(9–10), 973–978.
- Scotford, D. M. (1969). Metasomatic augen gneiss in greenschist facies, western Turkey. *Geological Society of America Bulletin*, 80(6), 1079–1094. [https://doi.org/10.1130/0016-7606\(1969\)80\[1079:MAGIGF\]2.0.CO;2](https://doi.org/10.1130/0016-7606(1969)80[1079:MAGIGF]2.0.CO;2)
- Scott, R. B., Bachinski, S. W., Nesbitt, R. W., & Scott, M. R. (1971). Rate of Al-Si ordering in sanidines from an ignimbrite cooling unit. *American Mineralogist: Journal of Earth and Planetary Materials*, 56(7–8), 1208–1221.
- Smith, J. V., & Brown, W. L. (1988). *Feldspar Minerals, Volume 1, Crystal Structures, Physical, Chemical, and Microtextural Properties*. New York: Springer-Verlag.
- Sorescu, M., Xu, T., & Diamandescu, L. (2010). Synthesis and characterization of $x\text{TiO}_2(1-x)(\alpha\text{-Fe}_2\text{O}_3)$ magnetic ceramic nanostructure system. *Materials Characterization*, 61(11), 1103–1118. <https://doi.org/10.1016/j.matchar.2010.07.004>
- Stanjek, H., & Schwertmann, U. (1992). The influence of aluminum on iron oxides. Part XVI: Hydroxyl and aluminum substitution in synthetic hematites. *Clays and Clay Minerals*, 40, 347–354.
- Stękiel, M., Przeniosło, R., Sosnowska, I., Fitch, A., Jasiński, J. B., Lussier, J. A., & Bieringer, M. (2015). Lack of a threefold rotation axis in $\alpha\text{-Fe}_2\text{O}_3$ and $\alpha\text{-Cr}_2\text{O}_3$ crystals. *Acta Crystallographica Section B*, 71(2), 203–208. <https://doi.org/10.1107/S205252061500342X>
- Stewart, D., & Ribbe, P. (1969). Structural explanation for variations in cell parameters of alkali feldspar with Al/Si ordering. *American Journal of Science*, 267, 444–462.
- Stewart, D., & Wright, T. (1974). Al/Si order and symmetry of natural potassic feldspars, and the relationship of strained cell parameters to bulk composition. *Bulletin de Mineralogie*, 97(2), 356–377.
- Thompson, P., Cox, D. E., & Hastings, J. B. (1987). Rietveld refinement of Debye-Scherrer synchrotron X-ray data from Al_2O_3 . *Journal of Applied Crystallography*, 20(2), 79–83. <https://doi.org/10.1107/S0021889887087090>
- Treiman, A. H., Bish, D. L., Vaniman, D. T., Chipera, S. J., Blake, D. F., Ming, D. W., et al. (2016). Mineralogy, provenance, and diagenesis of a potassic basaltic sandstone on Mars: CheMin X-ray diffraction of the Windjana sample (Kimberley area, Gale Crater). *Journal of Geophysical Research: Planets*, 121, 75–106. <https://doi.org/10.1002/2015JE004932>
- Walter, J. M., Iezzi, G., Albertini, G., Gunter, M. E., Piochi, M., Ventura, G., et al. (2013). Enhanced crystal fabric analysis of a lava flow sample by neutron texture diffraction: A case study from the Castello d'Ischia dome. *Geochemistry, Geophysics, Geosystems*, 14, 179–196. <https://doi.org/10.1029/2012GC004431>
- Wang, J., White, W. B., & Adair, J. H. (2005). Optical properties of hydrothermally synthesized hematite particulate pigments. *Journal of the American Ceramic Society*, 88(12), 3449–3454. <https://doi.org/10.1111/j.1551-2916.2005.00643.x>
- Wells, M., Gilkes, R., & Fitzpatrick, R. W. (2001). Properties and acid dissolution of metal-substituted hematites. *Clays and Clay Minerals*, 49(1), 60–72. <https://doi.org/10.1346/CCMN.2001.0490105>
- Wolfe, E. W., Wise, W. S., & Dalrymple, G. B. (1997). *The Geology and Petrology of Mauna Kea Volcano, Hawaii: A Study of Postshield Volcanism, U.S. Geological Survey Prof. Paper 1557* (p. 129). Washington: U.S. Government Printing Office.
- Yen, A. S., Ming, D. W., Vaniman, D. T., Gellert, R., Blake, D. F., Morris, R. V., et al. (2017). Multiple stages of aqueous alteration along fractures in mudstone and sandstone strata in Gale Crater, Mars. *Earth and Planetary Science Letters*, 471, 186–198. <https://doi.org/10.1016/j.epsl.2017.04.033>
- Yen, A. S., Morris, R. V., Gellert, R., Berger, J. A., Sutter, B., Downs, R. T., et al. (2017). Hydrothermal signatures at Gale Crater, Mars, and possible in-situ formation of tridymite. American Geophysical Union Fall Meeting, New Orleans, LA, Abstract #P24B-04.
- Zhou, L., Guo, J., Liu, B., & Li, L. (2001). Structural state of adularia from Hishikari, Japan. *Chinese Science Bulletin*, 46(11), 950–953. <https://doi.org/10.1007/BF02900474>